Materials Today Sustainability 35 (2026) 101422

Contents lists available at ScienceDirect

Materials Today Sustainability

journal homepage: www.journals.elsevier.com/materials-today-sustainability

Balancing defect formation and electronic coherence in CO_2-activated carbon nitride for efficient visible-light water purification

Gregor Žerjav [a,*,1], Matevž Roškarič [a,1], Andraž Mavrič [b], Miklós Németh [c], Albin Pintar [a,**]

[a] Department of Inorganic Chemistry and Technology, National Institute of Chemistry, Hajdrihova ulica 19, Ljubljana, SI-1001, Slovenia
[b] Materials Research Laboratory, University of Nova Gorica, Vipavska cesta 13, Nova Gorica, SI-5000, Slovenia
[c] HUN-REN Centre for Energy Research, Institute for Energy Security and Environmental Safety, Department of Surface Chemistry and Catalysis, Konkoly-Thege M. street 29-33, Budapest, H-1121, Hungary

ARTICLE INFO

Keywords:
Graphitic carbon nitride
CO_2-Assisted activation
Defect-coherence crossover
Reactive oxygen species
Visible-light photocatalysis
Photocatalytic pollutant degradation

ABSTRACT

CO_2-assisted thermal activation provides a scalable and sustainable strategy for controlled defect engineering of graphitic carbon nitride (g-C_3N_4) without chemical doping or templating. In this work, CO_2-treated g-C_3N_4 materials activated between 500 and 675 °C were investigated for visible-light-driven degradation of bisphenol pollutants in water. Progressive CO_2 etching induced layer thinning, porosity development, moderate nitrogen depletion, and band-gap narrowing, while largely preserving the heptazine framework up to 650 °C. The optimally activated sample (CN650) exhibited near-complete mineralisation of bisphenol An under simulated solar irradiation, achieving 91% TOC removal and substantially enhanced photocatalytic performance compared with pristine g-C_3N_4. Combined structural, spectroscopic, and photoelectrochemical analyses revealed a non-monotonic relationship between defect density, reactive oxygen species generation, and photocatalytic activity. Although excessive activation at 675 °C promoted enhanced superoxide radical formation, it simultaneously compromised the preservation of long-range electronic coherence and reduced effective charge utilisation. In contrast, optimal photocatalytic performance was achieved through a balanced interplay between defect-assisted oxygen activation and the preservation of long-range electronic coherence. The findings demonstrate that photocatalytic efficiency is governed not simply by surface area or radical density, but by the coupling between defect formation and charge-carrier utilisation. Furthermore, the optimally activated CN650 photocatalyst exhibited excellent structural stability and retained its photocatalytic performance over five consecutive reuse cycles. Overall, this work establishes CO_2-assisted activation as a scalable and sustainable strategy for designing high-performance metal-free photocatalysts for visible-light-driven water purification.

1. Introduction

The increasing release of persistent organic pollutants into aquatic environments poses a major threat to ecosystems and human health. Among these contaminants, bisphenol A (BPA) and its structural analogues, such as bisphenol F (BPF), bisphenol S (BPS), and bisphenol AF (BPAF), are of particular concern due to their endocrine-disrupting activity, high chemical stability, and widespread industrial use [1], [2]. These compounds are consistently detected in surface water, groundwater, and even drinking water sources, reflecting their resistance to conventional biological and physicochemical treatment processes [2]. Conventional wastewater treatment methods are often ineffective for the complete removal of these compounds, prompting the development of advanced oxidation processes capable of mineralising recalcitrant organic pollutants under mild conditions [3–6].

Photocatalysis driven by solar or visible light has emerged as a promising and sustainable approach for water remediation [7]. By utilising renewable solar energy, photocatalytic processes transform organic contaminants without the addition of chemical oxidants, thereby minimising secondary pollution and operational costs. In this context, graphitic carbon nitride (g-C_3N_4) has attracted considerable attention as a metal-free photocatalyst owing to its suitable band gap (~2.6-2.7 eV), chemical stability, low toxicity, and facile synthesis from earth-abundant, nitrogen-rich precursors [8–11]. g-C_3N_4 has been

* Corresponding author.
** Corresponding author.
E-mail addresses: gregor.zerjav@ki.si (G. Žerjav), albin.pintar@ki.si (A. Pintar).
[1] Both authors contributed equally to this work.

https://doi.org/10.1016/j.mtsust.2026.101422
Received 27 May 2026; Received in revised form 6 July 2026; Accepted 21 July 2026
Available online 24 July 2026

widely investigated for photocatalytic water splitting, CO_2 reduction, and degradation of organic pollutants, highlighting its versatility as a visible-light-responsive semiconductor [12–14]. Additionally, the polymeric nature of g-C_3N_4 allows extensive structural and electronic tunability, making it a particularly attractive platform for rational catalyst design [15], [16]. However, the practical application of pristine g-C_3N_4 is severely limited by its low specific surface area, strong interlayer stacking, limited light-harvesting capability, and rapid recombination of photogenerated charge carriers [8–10].

To overcome these intrinsic limitations, extensive efforts have focused on modifying g-C_3N_4 through heteroatom doping, heterojunction construction, defect engineering, morphology control and band-gap engineering [15–18]. Similar defect-engineering strategies have also been successfully applied to graphene-, transition-metal dichalcogenide (TMDC)-, and metal oxide-based photocatalysts to improve visible-light absorption, charge separation, and photocatalytic activity through rational modulation of the electronic structure and interfacial charge-transfer processes [19–21]. While these approaches can significantly enhance photocatalytic performance, many rely on multistep syntheses, foreign elements, or complex architectures that limit scalability and practical implementation. Among these strategies, post-synthetic thermal exfoliation and etching have emerged as particularly effective and scalable, enabling simultaneous tuning of crystallinity, porosity, and electronic structure without introducing foreign elements [22], [23]. Thermal treatment can induce layer thinning, pore formation, and partial framework decomposition, which collectively enhance surface area, expose new active sites, and improve charge transport [24].

Importantly, the gaseous atmosphere employed during thermal treatment plays a decisive role in determining the physicochemical properties and photocatalytic performance of g-C_3N_4 [25]. While air and inert atmospheres mainly promote oxidative exfoliation or limited defect formation, recent studies have shown that CO_2 acts as a unique and mild activating agent, inducing selective etching, vacancy-related surface defects, and modified surface chemistry [19,26]. Unlike aggressive chemical activation routes, CO_2 activation enables controlled framework modification while preserving the metal-free nature and chemical integrity of carbon nitride. Previous studies have demonstrated that thermal treatment under different gaseous atmospheres (air, inert gases, and CO_2) results in markedly different structural evolution and photocatalytic behaviour of g-C_3N_4. Building upon these findings, the present work focuses exclusively on CO_2-assisted activation to establish a comprehensive structure-property-activity relationship as a function of activation temperature. In particular, CO_2 calcination has been shown to outperform air and N_2 atmospheres in photocatalytic hydrogen evolution and pollutant degradation due to improved charge-carrier dynamics and interlayer electron transport. Specifically, Vega et al. [19] reported that CO_2-assisted thermal treatment of g-C_3N_4 increases the specific surface area and partially reduces crystallinity, resulting in significantly enhanced photocatalytic hydrogen evolution compared to bulk g-C_3N_4. This improvement was attributed to controlled CO_2-induced etching, which disrupts long-range order while preserving the heptazine framework and increasing the density of accessible surface sites. Similarly, Gaidi et al. [20] showed that thermally exfoliated g-C_3N_4 nanosheets exhibit improved visible-light absorption and charge-carrier separation, leading to enhanced degradation of organic pollutants through increased formation of reactive oxygen species. Together, these studies indicate that the photocatalytic performance of CO_2-activated g-C_3N_4 depends on balancing structural activation with preservation of electronic connectivity [17,18]. However, the relationship between activation-induced structural evolution, electronic coherence, and reactive oxygen species generation remains insufficiently understood. In the present work, the term electronic coherence is used to describe the preservation of long-range electronic communication within the π-conjugated carbon nitride framework, which enables efficient charge transport and suppresses carrier trapping despite the introduction of activation-induced defects. It does not refer to quantum coherence, but rather to the ability of the extended conjugated network to sustain efficient migration of photogenerated charge carriers across the framework.

Morphology-controlled g-C_3N_4, particularly thermally exfoliated or partially etched nanosheets, has been reported to exhibit enhanced adsorption capacity, improved separation of photogenerated charge carriers, and increased generation of reactive oxygen species (ROS), such as superoxide radicals and singlet oxygen, which are critical for efficient photocatalytic degradation of organic pollutants [12,20,27]. The balance between surface area, defect density, and electronic structure is therefore crucial, as excessive etching or framework collapse can be detrimental to photocatalytic activity [17,18]. Despite these advances, most existing studies focus primarily on hydrogen evolution or model dye degradation, while systematic investigations correlating CO_2-induced structural evolution with reactive oxygen species generation and degradation of environmentally relevant micropollutants remain scarce [19]. Furthermore, the combined influence of CO_2 treatment temperature on porosity development, band gap modulation, surface acid-base properties, and photocatalytic reaction pathways has not yet been comprehensively elucidated.

Notably, unlike previous studies that primarily reported enhanced photocatalytic activity following CO_2-assisted activation, the present work systematically identifies the transition from beneficial defect formation to excessive framework degradation. By systematically varying the CO_2 treatment temperature (500-675 °C), we identify a defect-coherence crossover, where increasing defect density initially enhances charge separation and oxygen activation, whereas excessive activation progressively compromises the preservation of long-range electronic coherence and limits photocatalytic efficiency. To identify not only the optimum activation conditions but also the onset of excessive framework degradation, the activation series was intentionally extended to 675 °C, where structural collapse was expected to occur. By combining structural, spectroscopic, photoelectrochemical, and photocatalytic analyses over a broad activation-temperature range, we demonstrate that photocatalytic performance is governed not simply by defect density or surface area, but by the balance between activation-induced defect formation and the preservation of long-range electronic coherence within the carbon nitride framework. This establishes a general structure-property-activity relationship for CO_2-activated metal-free photocatalysts.

2. Experimental

2.1. Catalyst synthesis

Bulk carbon nitride (CN) was prepared by thermal polycondensation of dicyandiamide (DCDA). Typically, 2.0 g of DCDA was placed in an alumina crucible and calcined in a muffle furnace under ambient air by heating to 550 °C at a rate of 300 °C h^{-1} and holding for 4 h. After natural cooling to room temperature, the resulting yellow solid was collected and designated as CN. CO_2-treated carbon nitride samples (CNXXX) were obtained by secondary thermal treatment of CN under a continuous CO_2 flow at controlled temperature. Briefly, 1.5 g of CN was loaded into a rectangular MgO crucible and placed in a quartz tubular furnace. The system was purged with pure CO_2 (purity 4.8) at room temperature for 15 min prior to heating. The samples were then heated to the desired final temperatures (500, 550, 600, 625, 650, or 675 °C) at a rate of 120 °C h^{-1}, maintained for 1 h, and cooled naturally to room temperature under a continuous CO_2 flow of 30 L h^{-1}. The resulting materials were labelled CN500, CN550, CN600, CN625, CN650, and CN675, respectively. Thermal treatment at 700 °C resulted in complete decomposition of the carbon nitride framework, yielding no recoverable solid.

2.2. Physicochemical and spectroscopic characterisation

The crystalline structure of the materials was analysed by X-ray diffraction (XRD) using Cu Kα radiation. Morphology and microstructure were examined by scanning electron microscopy (SEM) and transmission electron microscopy (TEM), including high-resolution TEM (HRTEM) and energy-dispersive X-ray spectroscopy (EDS) for elemental analysis. Textural properties, including specific surface area and pore size distribution, were determined by N_2 physisorption measurements (BET method). Skeleton density and total pore volume were evaluated by helium pycnometry. Surface acidity and basicity were quantified by pyridine-TPD and CO_2-TPD, respectively, while thermal stability was assessed by thermogravimetric analysis (TGA). Surface chemical composition and electronic states were investigated by X-ray photoelectron spectroscopy (XPS), with binding energies referenced to the C 1s signal at 284.8 eV. Optical properties were characterised by UV-Vis diffuse reflectance spectroscopy (DRS). Steady-state and time-resolved photoluminescence (PL and TCSPC) measurements were performed to analyse charge-carrier dynamics. Electron paramagnetic resonance (EPR) spectroscopy was used to detect intrinsic paramagnetic defects and photoinduced reactive oxygen species (ROS). These complementary techniques were selected to establish structure-property-activity relationships and to elucidate the electronic and surface modifications induced by CO_2 treatment, particularly regarding defect formation, charge-carrier dynamics, and reactive oxygen species generation under visible-light irradiation. Detailed instrumental parameters, data acquisition settings, and fitting procedures are provided in the Supplementary information.

2.3. Photoelectrochemical characterisation

Photoelectrochemical measurements were conducted using a conventional three-electrode configuration in 0.5 M Na_2SO_4 aqueous electrolyte under visible-light irradiation using a Schott KL 2500 LED lamp (emission spectrum shown in Fig. S1a). Impedance spectra were analysed by fitting the Nyquist plots to an equivalent circuit comprising solution resistance (R_S), charge-transfer resistance (R_{CT}), and a constant phase element (CPE). Further details regarding electrode preparation, instrumental settings, and data fitting are provided in the Supplementary information.

2.4. Photocatalytic activity tests

Photocatalytic oxidation experiments under simulated solar irradiation were carried out using a Sciencetech SciSun Series arc lamp system operated at 1 Sun intensity (emission spectrum shown in Fig. S1b). The reactions were performed in a bottom-flat electrochemical glass reactor thermostatted at 20 °C with a Julabo F25/ME circulating thermostat. Bisphenol A (BPA, Aldrich, purity ≥99.0%) was selected as the primary model organic pollutant at an initial concentration of 10 mg L^{-1} (0.0438 mM). The photocatalyst concentration was set at 125 mg L^{-1} in 100 mL of the aqueous pollutant solution, with continuous stirring at 400 rpm and an airflow rate of 7.2 L h^{-1}. Before illumination, the suspension was kept in the dark for 30 min to ensure adsorption-desorption equilibrium. In addition to BPA, the degradation of structurally related bisphenol analogues (bisphenol F (BPF), bisphenol S (BPS), and bisphenol AF (BPAF)) was investigated under identical experimental conditions. In all cases, the initial concentrations of the analogues were adjusted to be equimolar with respect to BPA. During irradiation, liquid-phase samples were withdrawn at predetermined intervals and filtered through 0.2 μm regenerated cellulose membrane filters before analysis. The selected photocatalytic conditions were based on our previous optimisation studies [1,9,11] and commonly reported protocols for visible-light photocatalytic degradation of bisphenol pollutants. The catalyst loading, initial pollutant concentration, airflow rate, reaction volume, and irradiation conditions were chosen to ensure reproducible photocatalytic testing, continuous oxygen supply throughout the reaction, and direct comparison among all investigated photocatalysts under identical experimental conditions.

To elucidate the role of reactive species involved in the photocatalytic process, a series of quenching experiments was conducted using the same reactor configuration and the CN600 and CN650 catalyst samples. p-Benzoquinone (BQ), sodium azide (NaN_3), methanol (MeOH), disodium ethylenediaminetetraacetate (NaEDTA), and formic acid (HCOOH) were employed as scavengers for superoxide anion radicals ($^{\bullet}O_2^-$), singlet oxygen ($^1O_2$), hydroxyl radicals ($^{\bullet}OH$), and photogenerated holes (h^+), respectively. In all cases, the scavenger concentration was maintained at 10 mM.

The concentrations of BPA, BPF, BPAF, and BPS were determined by HPLC using a Shimadzu LC-40 system equipped with a BDS Hypersil C18 column (100 × 4.6 mm, 2.4 μm) and PDA detection (190-350 nm). Methanol/water mixtures were used as the mobile phase (70:30, v/v for BPA and BPAF; 60 vol% methanol for BPS and BPF), with flow rates of 0.3-0.5 mL min^{-1}. The column and autosampler temperatures were maintained at 30 °C and 25 °C, respectively.

Total organic carbon (TOC) content in liquid-phase samples was quantified using a Shimadzu TOC-L analyser equipped with an ASI-L autosampler, with synthetic air (Messer) employed as the oxidising gas. The analytical uncertainty, determined from three replicate measurements, was within ±1%. Elemental carbon, nitrogen, and hydrogen contents of fresh and spent photocatalysts were measured using a PerkinElmer CHNS 2400 Series II analyser.

Recycling experiments were conducted to assess the stability and reusability of the selected photocatalyst. After each 120-min irradiation run, the suspension was filtered through a 0.2 μm regenerated cellulose membrane filter. The recovered catalyst was thoroughly washed with ultrapure water to remove residual organic species, dried at 60 °C overnight, and reused under identical experimental conditions in a fresh pollutant solution. No additional thermal regeneration or reductive treatment was applied between cycles.

3. Results and discussion

3.1. Structural and textural characterisation of CO_2-treated g-C_3N_4

The structural evolution of g-C_3N_4 during CO_2-assisted thermal treatment was first examined by X-ray diffraction (Fig. 1, Table 1). Pristine CN displays two characteristic reflections at $2\theta \approx 13.22°$ and 27.42°, corresponding to the (100) in-plane periodic arrangement of heptazine units and the (002) interlayer stacking of conjugated aromatic layers [28], [29]. After CO_2 treatment at moderate temperatures (500-600 °C), both reflections remain observable but exhibit gradual shifts and peak broadening. The (100) peak shifts slightly to higher 2θ values, corresponding to a decrease in the in-plane spacing from 0.669 to ~0.660 nm, indicating local rearrangement within the heptazine planes during the early stages of activation. Simultaneously, the crystallite size decreases from 5.8 to ~4-5 nm, suggesting progressive loss of long-range in-plane coherence. For CN625, the (100) reflection shifts further and significantly decreases in intensity, indicating substantial disruption of planar periodicity. At 650 °C, the (100) reflection disappears, suggesting the predominance of edge sites and short heptazine fragments rather than extended periodic domains. In contrast, the (002) reflection remains detectable up to CN650 but progressively broadens and shifts to lower angles, corresponding to expansion of the interlayer spacing and pronounced thinning of stacked domains. The progressive broadening and shift of the (002) reflection indicate weakening of interlayer interactions and partial exfoliation, whereas complete disappearance of both reflections at 675 °C confirms collapse of the carbon nitride framework.

The crystallographic trends identified by XRD are reflected in the morphological evolution observed by SEM and TEM. SEM micrographs of pristine CN (Fig. 2, S2 and S3) reveal dense agglomerates composed of

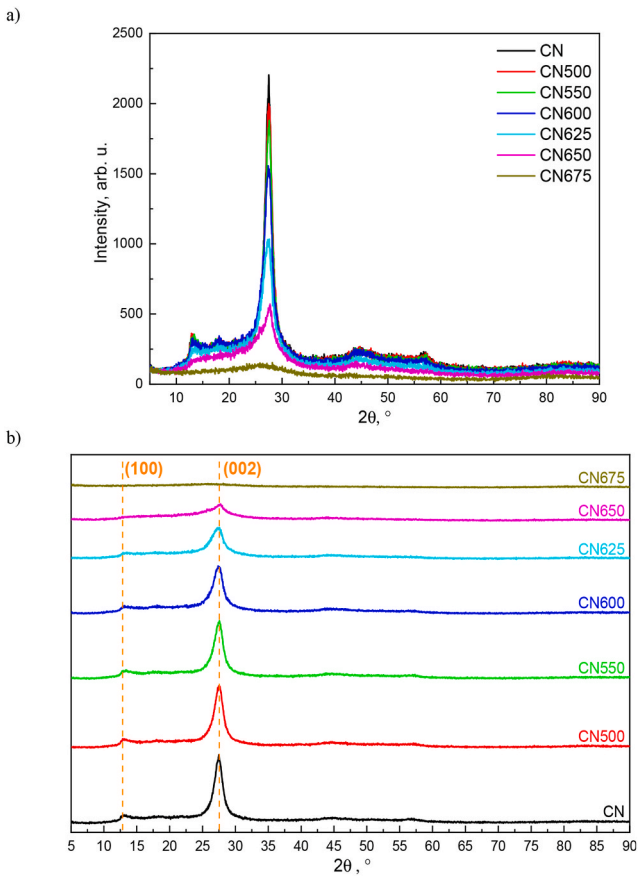

Fig. 1. X-ray diffraction (XRD) patterns of pristine and CO_2-activated g-C_3N_4 samples: a) full diffraction patterns, and b) stacked patterns highlighting the characteristic (100) and (002) reflections (according to ICDD 00-066-081), illustrating the progressive structural evolution induced by CO_2-assisted thermal treatment.

Table 1
XRD-derived structural parameters of pristine and CO_2-activated g-C_3N_4 samples, including peak positions (2θ), interplanar spacings (d), and crystallite sizes for the (100) in-plane and (002) interlayer reflections.

Sample	(100)			(002)		
	2θ	d-spacing	Crystallite size	2θ	d-spacing	Crystallite size
	°	nm	nm	°	nm	nm
CN	13.22	0.669	5.8	27.42	0.325	5.5
CN500	13.28	0.666	5.7	27.45	0.325	5.1
CN550	13.41	0.660	4.4	27.43	0.325	5.0
CN600	13.39	0.661	5.0	27.35	0.326	4.5
CN625	13.59	0.651	2.6	27.23	0.327	4.0
CN650	n.d.	n.d.	n.d.	27.05	0.329	2.0
CN675	n.d.	n.d.	n.d.	n.d.	n.d.	n.d.

n.d. - not determined.

thick, strongly stacked layers with limited surface accessibility, consistent with the pronounced (002) reflection. After CO_2 treatment at 500-550 °C, the overall morphology remains largely agglomerated, but surface fissures and partially delaminated regions appear, indicating the onset of structural loosening and weakening of interlayer contacts. From CN600 onwards, the materials progressively evolve into thinner and rougher nanosheets, indicating advanced exfoliation of the layered framework. At 650 °C, the morphology changes markedly: CN650 consists of fragmented and perforated nanosheets with irregular internal voids, suggesting that CO_2-induced etching occurs throughout the layered structure rather than only at the external surface. TEM and HRTEM images confirm progressive thinning of stacked domains, culminating in perforated nanosheets for CN650.

ATR-FTIR spectra of pristine and CO_2-treated g-C_3N_4 samples (Fig. 3a) provide insight into the evolution of surface functional groups during thermal activation. All samples exhibit the characteristic vibrational features of polymeric g-C_3N_4, indicating that the heptazine-based framework is largely preserved over a wide range of treatment temperatures. The broad band at 2700-3500 cm^{-1}, attributed predominantly to the stretching vibrations of terminal –NH/–NH_2 groups, with a minor contribution from adsorbed water and surface hydroxyl-related species, progressively decreases with increasing activation temperature, reflecting gradual removal of terminal –NH_x groups during thermal treatment [30]. This trend is consistent with CHN analysis, which shows a decrease in hydrogen content up to CN600-CN625. In the fingerprint region, strong bands between 1200 and 1650 cm^{-1} corresponding to C–N–C and C=N stretching within the heptazine units remain largely unchanged [31], confirming that CO_2 activation does not disrupt the fundamental chemical structure of g-C_3N_4. The characteristic heptazine breathing mode at 805 cm^{-1} remains clearly visible up to CN650, despite extensive exfoliation and porosity development. In contrast, this band becomes broadened for CN675, indicating increased structural disorder. No additional bands associated with oxygen-containing functional groups are observed, confirming that CO_2 acts primarily as a selective activating agent rather than an oxidising atmosphere [23].

The evolution of textural properties induced by CO_2-assisted thermal activation was investigated by N_2 adsorption-desorption measurements, with the corresponding isotherms and pore size distributions shown in Fig. S7 and the quantitative parameters summarised in Table 2. Pristine CN exhibits low nitrogen uptake over the entire relative pressure range, consistent with its limited specific surface area (15 m^2 g^{-1}) and poorly developed porosity [26]. Similar behaviour is observed for CN500 and CN550, indicating that CO_2 treatment up to 550 °C does not significantly alter the accessible surface area or pore structure. A moderate increase in nitrogen uptake appears for CN600, accompanied by a slight rise in specific surface area (18 m^2 g^{-1}), suggesting the onset of internal structural opening. More pronounced changes occur for CN625, where nitrogen adsorption increases and a hysteresis loop characteristic of mesoporous materials becomes visible, indicating the formation of an interconnected mesoporous network resulting from CO_2-induced etching [23]. For CN650, the adsorption isotherm shows a steep increase in nitrogen uptake at intermediate relative pressures with a well-defined hysteresis loop, confirming extensive mesoporosity development [32]. The specific surface area increases sharply to 51 m^2 g^{-1} and the pore volume to 0.19 cm^3 g^{-1}. The average pore diameter remains relatively constant (~14 nm), suggesting that CO_2 activation promotes homogeneous expansion of internal porosity rather than uncontrolled macropore formation. At the highest treatment temperature (CN675), the specific surface area further increases to 117 m^2 g^{-1} with a pore volume of 0.22 cm^3 g^{-1}. However, this apparent improvement coincides with nitrogen loss and the disappearance of XRD reflections, indicating that the high surface area originates from framework fragmentation rather than controlled activation [33].

Helium pycnometry (Fig. S7c, Table 2) provides additional insight into the nature of the generated porosity. Despite the significant increase in surface area and pore volume from CN to CN650, the skeletal density remains nearly constant (~1.816-1.845 g cm^{-3}), whereas the bulk density decreases markedly from 0.430 to 0.135 g cm^{-3}. This behaviour indicates that CO_2 activation primarily induces internal void formation and structural thinning without extensive carbonisation of the carbon nitride framework. In contrast, reliable skeletal density values could not be obtained for CN675, confirming the loss of structural integrity at excessive activation temperatures.

The effect of CO_2-assisted thermal treatment on the elemental composition of g-C_3N_4 was analysed by CHN analysis (Table 2). Pristine CN exhibits carbon and nitrogen contents of 34.6 and 58.3 wt%,

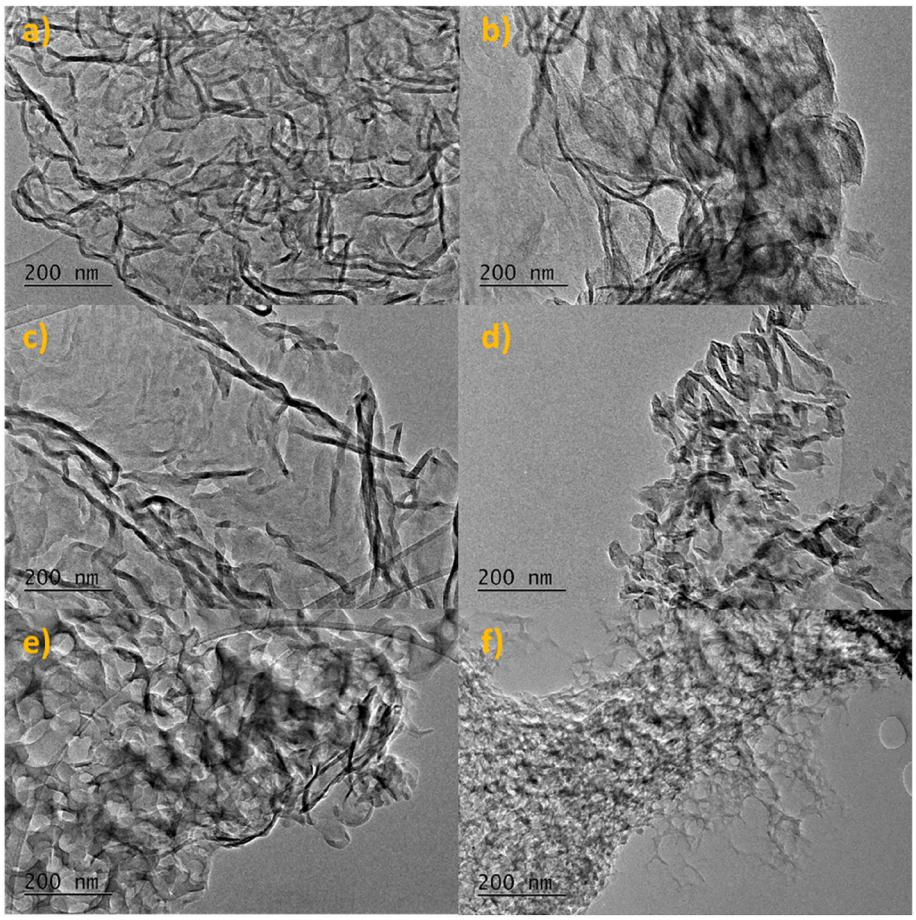

Fig. 2. TEM micrographs of dispersed g-C_3N_4 powders at different CO_2 activation temperatures: a) CN, b) CN500, c) CN550, d) CN600, e) CN650, and f) CN675. All images were acquired at comparable magnification (scale bar: 200 nm), illustrating the progressive exfoliation, perforation, and eventual structural degradation caused by CO_2-assisted thermal treatment.

respectively, consistent with the expected composition of polymeric carbon nitride [34]. Following CO_2 treatment up to 625 °C, the elemental composition remains largely unchanged, indicating that the fundamental g-C_3N_4 framework is preserved during moderate activation. In contrast, the hydrogen content decreases progressively from 2.1 wt% (CN) to 1.3 wt% (CN600), reflecting gradual removal of terminal –NH_x groups and weakly bound species during thermal treatment [35]. The decreasing hydrogen content indicates progressive removal of terminal NH_x groups during thermal treatment. At higher activation temperatures, a clear compositional change occurs. For CN650, the nitrogen content decreases to 55.4 wt%, indicating the onset of selective nitrogen depletion associated with extensive structural etching. This change coincides with the disappearance of the (100) XRD reflection and the strong increase in surface area. At 675 °C, the elemental composition changes markedly, with significant decreases in both nitrogen and carbon contents accompanied by an increase in hydrogen content. These results indicate severe framework degradation and partial carbonisation, consistent with the disappearance of characteristic XRD reflections, collapse of the layered morphology, and the loss of structural integrity confirmed by helium pycnometry [36].

Thermogravimetric analysis was used to evaluate the thermal stability of g-C_3N_4 after CO_2-assisted activation, with the characteristic decomposition temperatures (T_{50} and T_{90}) summarised in Table 3 (Fig. S8). Pristine CN exhibits T_{90} and T_{50} values of 607 and 642 °C, respectively, consistent with the thermal behaviour expected for polymeric carbon nitride [33]. For samples treated in CO_2 up to 600 °C, thermal stability remains largely preserved. CN500 and CN550 show slightly increased T_{50} and T_{90} values, likely due to partial condensation and removal of thermally labile terminal groups, while CN600 exhibits thermal behaviour comparable to pristine CN. At higher activation temperatures, a progressive decrease in thermal stability is observed. CN625 shows reduced decomposition temperatures, indicating the onset of structural weakening associated with exfoliation and porosity development. For CN675, T_{90} decreases drastically to 433 °C, confirming severe framework degradation. This behaviour is consistent with the disappearance of XRD reflections, nitrogen loss observed in CHN analysis, and the collapse of the layered morphology. Notably, the reference sample thermally treated in CO_2 without prior activation (CN-CO_2) exhibits significantly higher thermal stability, demonstrating that CO_2 itself does not destabilise the carbon nitride framework, while the reduced stability of highly activated samples originates from excessive etching and defect accumulation at elevated temperatures [30].

Overall, the combined XRD, ATR-FTIR, electron microscopy, textural, elemental, and thermogravimetric analyses reveal progressive CO_2-induced exfoliation, porosity development, and defect formation while largely preserving the heptazine framework up to CN650. In contrast, further activation at 675 °C results in significant framework degradation, as evidenced by the loss of crystallinity, nitrogen depletion, and reduced thermal stability. The CN-CO_2 reference confirms that CO_2 itself does not destabilise the carbon nitride framework. Collectively, these results identify CN650 as the structural optimum, providing the foundation for the subsequent evolution of the surface chemistry, electronic structure, and photocatalytic performance.

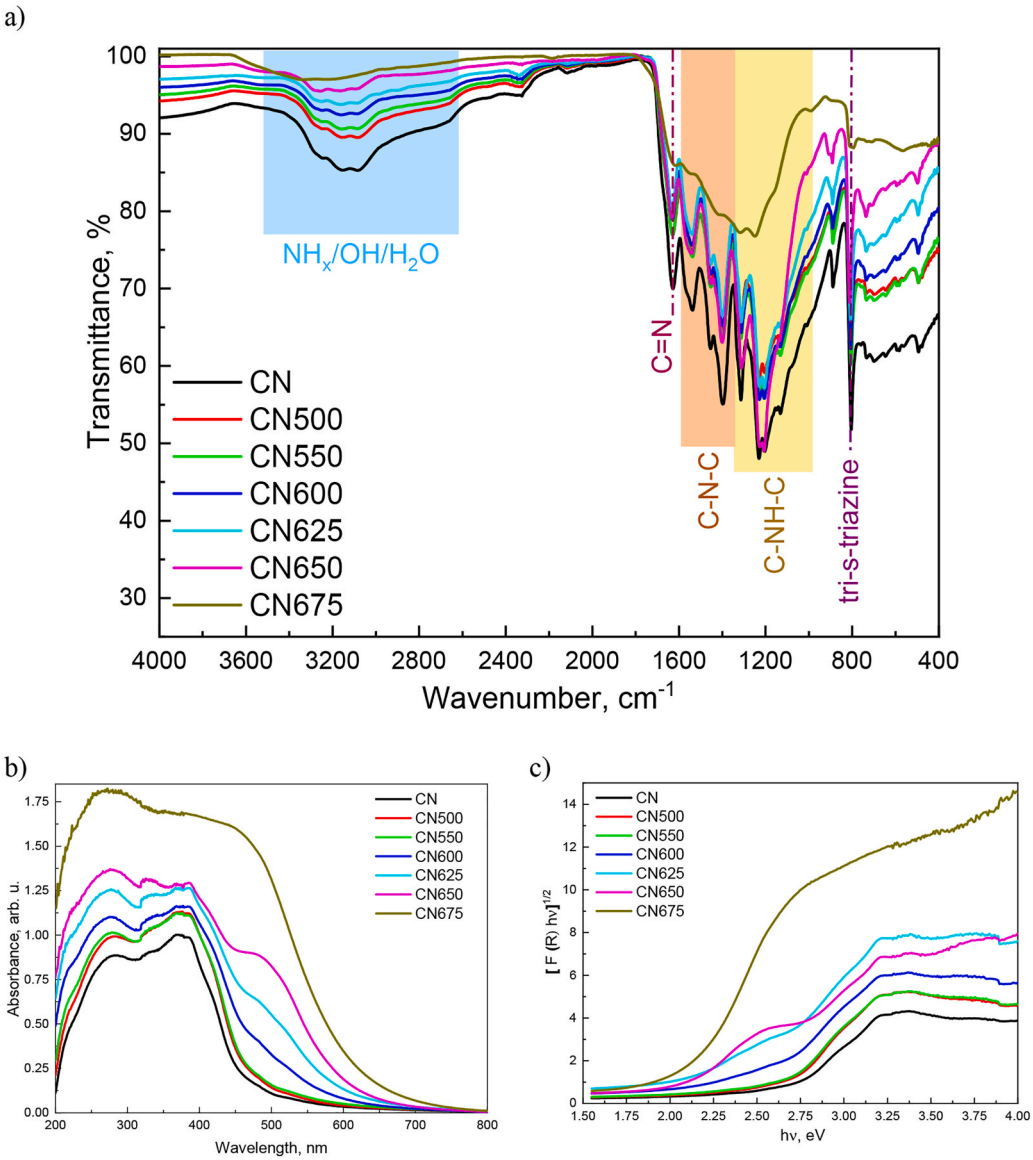

Fig. 3. a) ATR-FTIR spectra of pristine and CO_2-activated g-C_3N_4 samples, showing –NH_x/–OH stretching vibrations, C–NH–C/C=N/C–N–C stretching modes of the heptazine framework, and the characteristic tri-s-triazine breathing. UV-Vis diffuse reflectance spectra of pristine and CO_2-activated g-C_3N_4 samples: b) absorbance spectra and c) Kubelka-Munk-transformed Tauc plots for band gap estimation, illustrating the progressive red shift and band gap narrowing induced by CO_2-assisted thermal activation.

Table 2
Elemental composition (CHN), textural properties (specific surface area (S_{BET}), pore volume (V_{pore}), and pore size (d_{pore})), and density parameters of pristine and CO_2-activated g-C_3N_4 samples.

Sample	C	H	N	S_{BET}	V_{pore}	d_{pore}	Skeletal density	Average total pore volume	Bulk density
	%	%	%	m [2] g^{-1}	cm [3] g^{-1}	nm	g cm^{-3}	cm [3] g^{-1}	g L^{-1}
CN	34.6	2.1	58.3	15	0.06	15.1	1.835	1.78	0.430
CN500	34.9	1.7	58.9	15	0.06	15.5	1.821	2.14	0.372
CN550	35.2	1.6	58.9	16	0.06	15.7	1.816	1.94	0.402
CN600	35.3	1.3	58.5	18	0.06	14.6	1.825	2.44	0.334
CN625	35.4	1.5	58.1	21	0.08	14.9	1.838	3.10	0.274
CN650	34.6	1.5	55.4	51	0.19	14.2	1.845	6.88	0.135
CN675	31.6	1.9	47.9	117	0.22	7.5	n.d.	n.d.	n.d.

n.d. - not determined.

3.2. Surface chemical properties of CO_2-treated g-C_3N_4

X-ray photoelectron spectroscopy (XPS) was conducted to analyse the surface composition and electronic states of the pristine and CO_2-activated g-C_3N_4 samples. Survey spectra (Fig. S9) confirm that carbon and nitrogen remain the dominant surface elements up to 650 °C, with only minor oxygen contributions (1-2 at.%). In contrast, CN675 shows a marked increase in surface oxygen (6.6 at.%) along with detectable Na

Table 3
Thermal stability parameters derived from thermogravimetric analysis (T_{90} and T_{50}), surface acid-base properties obtained by pyridine- and CO_2-TPD (density of acidic surface sites, DAcSS; concentration of acidic surface sites, cAcSS; density of basic surface sites, DBaSS; concentration of basic surface sites, cBaSS), and charge-transfer resistance (R_{CT}) values determined from electrochemical impedance spectroscopy for pristine and CO_2-activated g-C_3N_4 samples.

Sample	T_{90}	T_{50}	DAcSS	cAcSS	DBaSS	cBaSS	R_{CT}
	°C	°C	mmol m^{-2}	mmol g^{-1}	mmol m^{-2}	mmol g^{-1}	MΩ
CN	607	642	0.0001	0.001	0.0040	0.060	0.498
CN500	615	641	n.d.	n.d.	n.d.	n.d.	n.d.
CN550	627	654	n.d.	n.d.	n.d.	n.d.	0.443
CN600	604	640	n.d.	n.d.	n.d.	n.d.	0.347
CN625	591	623	n.d.	n.d.	n.d.	n.d.	n.d.
CN650	533	610	0.0001	0.007	0.0055	0.279	0.403
CN675	433	613	n.d.	n.d.	n.d.	n.d.	0.416
CN CO_2	655	763	n.d.	n.d.	n.d.	n.d.	n.d.

n.d. - not determined.

and Ca signals, consistent with partial framework degradation and the formation of carbonate-related surface species at excessive activation temperatures. The Na 1s signal appears only for CN675, whereas the Ca 2p contribution becomes more evident for the highly activated CN650 and CN675 samples. These signals are attributed to trace inorganic impurities that become more readily detectable following framework thinning, nitrogen depletion, and mass loss during severe CO_2 activation. High-resolution N 1s spectra (Fig. 4a) display the characteristic dominant component at 398.7 eV, corresponding to sp^2-hybridised C–N=C species within the heptazine framework [37]. From CN to CN650, the overall spectral shape, binding energy positions, and peak envelopes remain largely preserved. Minor variations in the high-binding-energy region are not systematic and indicate that the surface chemical structure remains largely unchanged up to CN650. Only CN675 shows pronounced peak broadening and redistribution of spectral intensity, consistent with structural disorder and reduced electronic coherence. Similarly, the C 1s spectra (Fig. 4b) exhibit the typical graphitic carbon nitride features, including the main C–N_3 contribution at 288.2 eV and a π–π* shake-up satellite associated with extended aromatic conjugation [30,38]. Up to 650 °C, the relative spectral profile remains essentially unchanged, indicating preservation of the conjugated framework. In CN675, attenuation of the π–π* feature and increased C–O contributions (286 eV) further confirm disruption of the aromatic network. Quantitative analysis (Table S1) shows that the N/C ratio within the g-C_3N_4 framework remains in the narrow range 1.41-1.44 for CN-CN650. These results confirm that CO_2 activation up to CN650 preserves the chemical identity of the carbon nitride framework despite significant structural evolution. Valence band spectra were analysed to determine the valence band maximum (VBM) [39]. The optical band gap (E_g) values used in the subsequent analysis were independently obtained from UV-Vis diffuse reflectance spectroscopy (Tauc plots).

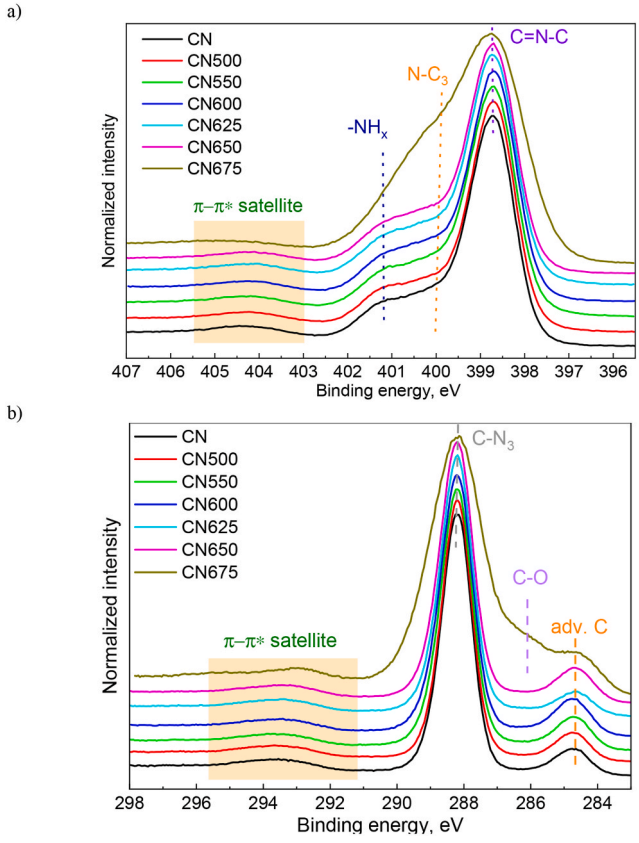

Fig. 4. Normalised high-resolution XPS spectra of a) N 1s and b) C 1s regions for pristine and CO_2-activated g-C_3N_4 samples. The spectral shape remains largely preserved up to 650 °C, whereas CN675 exhibits pronounced peak broadening, reduced π–π* intensity, and increased C–O contributions, indicating structural disorder at excessive activation temperatures.

Using the VBM and E_g values, the relative conduction band position was estimated (Table S2) according to [40]:

$$E_{CB} = E_{VB} - E_g \quad (1)$$

Here, E_{VB} refers to the valence band maximum determined by XPS, and E_g is the optical band gap obtained from UV-Vis diffuse reflectance spectroscopy (discussed in chapter 3.3). While the VBM remains nearly constant throughout the activation series, progressive band gap narrowing shifts the estimated conduction band position closer to the Fermi level (E_F). Because E_{VB} is referenced to E_F, the calculated E_{CB} values reflect relative energetic trends rather than absolute redox potentials [36]. The absence of significant valence band shifts, together with preserved surface stoichiometry up to CN650, indicates that CO_2 activation primarily induces defect-assisted electronic modulation rather than extensive chemical reconstruction. Together with XRD and CHN analyses, the XPS results confirm preservation of the carbon nitride framework up to CN650 despite pronounced electronic modulation arising from activation-induced defect formation.

The surface acid-base properties of selected g-C_3N_4 samples were quantified by pyridine-TPD and CO_2-TPD, with the results summarised in Table 3. Pristine CN shows a very low density of acidic sites (0.0001 mmol m^{-2}; 0.001 mmol g^{-1}), confirming the absence of significant Brønsted acidity and the predominantly neutral or weakly basic character of the carbon nitride surface. In contrast, a moderate concentration of basic sites is detected (0.0040 mmol m^{-2}; 0.060 mmol g^{-1}), consistent with the presence of Lewis basic nitrogen functionalities within the heptazine framework [35]. Following CO_2-assisted activation, a pronounced modification of surface basicity is observed for CN650. While the density of acidic sites remains essentially unchanged on an area-normalised basis (0.0001 mmol m^{-2}), their concentration per unit mass increases to 0.007 mmol g^{-1} as a direct consequence of the substantially increased accessible surface area. This confirms that CO_2 activation does not introduce new acidic functionalities but rather exposes existing surface sites. In contrast, both the density and concentration of basic surface sites increase markedly for CN650, reaching 0.0055 mmol m^{-2} and 0.279 mmol g^{-1}, respectively [34]. Importantly, the increase in basic site density per unit surface area demonstrates that the enhancement in surface basicity cannot be attributed solely to higher surface area, but reflects genuine chemical modification of the surface, including enrichment in Lewis basic nitrogen sites and the formation of oxygen-containing surface groups detected by XPS. This behaviour is consistent with CO_2-induced exfoliation and internal etching, which expose edge nitrogen atoms and

defect-associated coordination environments, as evidenced by XRD, SEM, and TEM analyses [41]. The absence of reliable TPD data for intermediate samples (CN500-CN625) and for CN675 is attributed to either insufficient surface accessibility (low-temperature-treated samples) or excessive structural degradation (CN675), which precludes meaningful quantification of surface acid-base sites under the applied experimental conditions.

The impact of CO_2-assisted thermal activation on the surface charge properties of g-C_3N_4 was examined using pH-dependent zeta potential measurements, providing insight into the electrostatic behaviour of the photocatalysts under aqueous conditions (Fig. S10). Zeta potential is a key parameter governing colloidal stability, adsorption of charged or polar organic molecules, and interfacial interactions with dissolved oxygen species during photocatalytic reactions [42]. Pristine CN exhibits a relatively negative surface charge over a broad pH range, reflecting the predominance of neutral and weakly basic nitrogen functionalities within the polymeric framework. Upon CO_2 activation, a systematic shift in the zeta potential curves is observed, with the point of zero charge (pH_{pzc}) displaced towards higher pH values [43]. This shift is most pronounced for CN650, indicating an increased contribution from exposed Lewis basic nitrogen sites and edge functionalities generated during CO_2-induced exfoliation and internal etching, as well as the formation of polar oxygen-containing surface groups detected by XPS, which can further contribute to water adsorption. The upward shift of pH_{pzc} implies that CO_2-activated samples, particularly CN650, possess a more positively charged or less negatively charged surface under near-neutral conditions compared to pristine CN. Importantly, the modified surface charge is not merely a consequence of increased surface area, but reflects genuine chemical restructuring of the surface nitrogen environments. In contrast, the CN675 sample exhibits markedly different zeta potential behaviour. Despite its high apparent surface area, the zeta potential curve shows a reduced or irregular shift of the pH_{pzc}, accompanied by a diminished magnitude of surface charge. This indicates loss of well-defined surface nitrogen functionalities and increased surface heterogeneity, consistent with severe framework degradation observed by XRD, CHN, and TGA. Rather than further enhancing electrostatic interaction with aqueous species, excessive CO_2 activation at this temperature leads to poorly defined surface charge characteristics, which are unfavourable for controlled adsorption and interfacial charge transfer. The modified surface charge is expected to promote adsorption of polar phenolic molecules and facilitate interfacial interactions with dissolved oxygen during photocatalysis [44]. The loss of a well-defined surface charge for CN675 therefore provides an additional electrostatic rationale for its inferior photocatalytic behaviour, despite its high surface area. Moreover, the modified electrostatic environment is expected to affect interaction with dissolved molecular oxygen, thereby influencing the formation and stabilisation of reactive oxygen species.

Collectively, CO_2-assisted thermal activation selectively enhances the surface basicity and electrostatic properties of g-C_3N_4 within a narrow activation window while preserving the chemical identity of the carbon nitride framework. The optimally activated CN650 sample combines increased Lewis basicity with favourable surface charge characteristics, providing a chemically and electrostatically optimised interface for photocatalytic reactions. In contrast, excessive activation at 675 °C leads to deterioration of the surface chemical and electrostatic properties as a result of framework degradation. Collectively, these results establish a direct link between CO_2-induced surface modification and the subsequent evolution of the electronic structure and charge-carrier dynamics discussed in the following section.

3.3. Optical and electronic properties of CO_2-activated g-C_3N_4

The optical response of the CO_2-activated g-C_3N_4 series was evaluated by UV-Vis diffuse reflectance spectroscopy (Fig. 3b). The spectra are presented in their original (non-normalised) form to illustrate the evolution of the diffuse optical response following CO_2 activation. The optical band-gap energies were determined exclusively from Kubelka-Munk transformed diffuse reflectance data using the Tauc method (Fig. 3c) and are summarised in Table S2 [45]. Pristine CN exhibits the characteristic absorption edge of polymeric g-C_3N_4, with an optical band gap of 2.74 eV, consistent with its visible-light activity [26], which is mainly limited to the near-UV/blue region. CO_2-assisted thermal activation induces a systematic red shift of the absorption edge and a pronounced enhancement of visible-light absorption. This trend is already apparent for CN500 and CN550, where the band gap decreases to 2.69 eV, indicating modest electronic structure modification at low activation temperatures. A much stronger effect is observed for higher-temperature treatments: E_g decreases progressively to 2.61 eV for CN600, 2.50 eV for CN625, and 2.38 eV for CN650. This gradual narrowing demonstrates that CO_2 activation continuously introduces electronic perturbations that extend light harvesting further into the visible region. In parallel with the band gap decrease, the absorbance spectra show an increasingly pronounced long-wavelength tail for CN600-CN650. Such sub-bandgap absorption is typically associated with defect-related states and increased structural disorder, which introduce mid-gap or band-tail levels that facilitate optical transitions at lower photon energies [30]. Together with XPS, these results indicate that CO_2 activation modifies the electronic structure primarily through activation-induced defect formation rather than chemical reconstruction. At the highest activation temperature, CN675 exhibits the strongest red shift and the smallest apparent band gap (2.15 eV), accompanied by very intense and broad visible-light absorption. However, this extreme optical response coincides with severe nitrogen loss (CHN), reduced thermal stability (TGA), and loss of crystallographic signatures (XRD), indicating that the pronounced band gap narrowing observed for CN675 likely reflects extensive framework disruption and the formation of highly disordered domains, accompanied by significant changes in the local bonding environment of the carbon-nitrogen network.

Excitation spectra (Fig. 5) further support the activation-induced evolution of the electronic structure. All samples display dominant excitation features centred at approximately 328 nm and within the 360-385 nm region (around 368 and 376 nm). The band at 328 nm corresponds to high-energy π–π* excitation within the heptazine-based conjugated framework, while the increasingly structured excitation response at 368-376 nm reflects an enhanced contribution from lower-energy electronic states closer to the band edge, commonly attributed to band-tail or defect-related states [26,30]. The pronounced splitting and shouldering of the 360-385 nm feature observed in highly activated samples (CN625-CN675) indicate the presence of multiple electronically distinct excitation channels, consistent with defect-assisted band gap narrowing and increased structural disorder inferred from UV-Vis diffuse reflectance analysis. Accordingly, excitation at 328 nm predominantly probes the intrinsic framework response, whereas excitation in the 368-376 nm range selectively addresses activation-induced sub-bandgap states, providing a rational basis for the excitation wavelengths used in the PL and TCSPC analysis.

To provide an integrated overview of the excitation-dependent photoluminescence behaviour, an excitation-emission matrix (EEM) was recorded for the representative optimally activated sample CN650 (Fig. S11). The EEM visualises the PL response across a broad excitation (339-387 nm) and emission (400-640 nm) wavelength range and reveals two dominant excitation regions centred at ~330 nm and 370-380 nm, both converging to a broad emission band spanning the blue-green region (460-500 nm). Importantly, both excitation channels lead to emission within the same spectral window, indicating that excited carriers relax toward a common emissive state before radiative recombination [34]. This excitation-emission continuity supports the interpretation that CO_2 activation primarily modifies charge-carrier relaxation dynamics through controlled defect-assisted electronic tuning.

Steady-state photoluminescence spectra recorded under excitation at

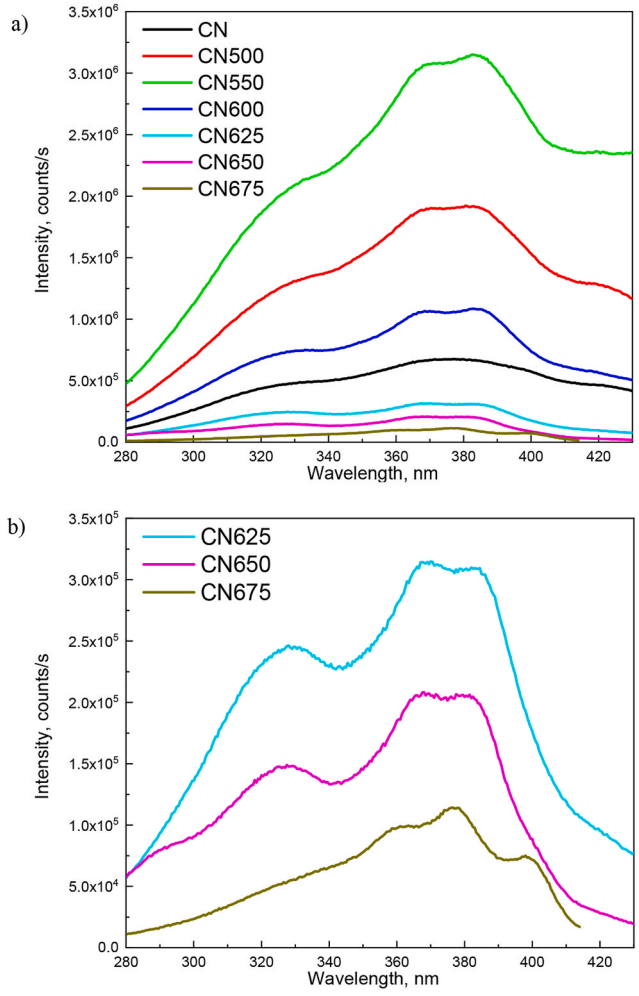

Fig. 5. Excitation spectra of pristine CN and CO_2-treated samples calcined at different temperatures: a) complete temperature series (CN-CN675), and b) enlarged view of high-temperature samples (CN625-CN675).

328 nm and in the 364-376 nm range are shown in Fig. S12. Under excitation at 328 nm, which predominantly probes near-band-edge electronic transitions, pristine CN and moderately activated samples (CN500-CN600) exhibit a broad emission band centred at 460-480 nm, characteristic of intrinsic radiative recombination in polymeric g-C_3N_4 [46]. With increasing CO_2 activation temperature, a pronounced quenching of PL intensity is observed, particularly for CN625-CN675, indicating the progressive opening of non-radiative relaxation pathways that affect even intrinsically excited charge carriers [47]. In contrast, excitation in the 364-376 nm region predominantly probes defect-related electronic states associated with band-tail levels formed during CO_2-assisted activation of the carbon nitride framework [48]. Under these conditions, the PL response becomes markedly more sensitive to activation temperature. CN600 exhibits the highest emission intensity, suggesting the presence of electronically accessible defect states that still support radiative relaxation. For CN650 and CN675, the emission intensity is strongly suppressed and the spectral features become less well defined, reflecting increased structural and electronic disorder and rapid non-radiative depopulation of defect-assisted excited states.

To further analyse the evolution of individual emission contributions, the steady-state PL spectra recorded under excitation in the 364-376 nm range were deconvoluted using a multi-Gaussian fitting procedure (Fig. S13), and the extracted peak positions and relative areas are summarised in Table S3 [49]. For all samples, the PL response is consistently described by four overlapping emission components located at approximately 405.9-407.9 nm (peak 1), 433.4-459.9 nm (peak 2), 452.4-486.4 nm (peak 3), and 496.7-526.5 nm (peak 4). The persistence of these components across the entire temperature series indicates that CO_2-assisted activation does not introduce new emissive states but instead redistributes the contribution of existing radiative relaxation pathways. While the peak positions remain largely invariant with activation temperature, the relative peak areas show pronounced and systematic changes. Moderately activated samples (CN500-CN550) display an increased contribution from intermediate- and low-energy emission components (peaks 2-4), reflecting enhanced population of defect- and edge-associated emissive channels [50]. For CN625 and CN650, the areas of peaks 2 and 3 decrease sharply, while for CN675 all emissive components are strongly diminished, resulting in weak and poorly resolved PL spectra. This redistribution and eventual loss of emissive contributions demonstrate that PL quenching induced by CO_2 activation originates from progressive depopulation of radiative relaxation pathways rather than from spectral transformation or formation of new emitting states. Low-temperature PL measurements (77 K, Fig. S14) confirm that the room-temperature PL quenching originates from enhanced non-radiative relaxation rather than elimination of emissive states [51].

Time-correlated single-photon counting (TCSPC) measurements were performed to elucidate the influence of CO_2-assisted thermal activation on the intrinsic charge-carrier recombination dynamics of g-C_3N_4. Representative decay profiles recorded under pulsed excitation are shown in Fig. S15–S17, and the corresponding fitting parameters are summarised in Table S4. For all samples investigated, the PL decays are well described by multi-exponential functions dominated by a fast decay component in the sub-nanosecond time regime ($\tau_1 \sim$ 0.46-2.54 ns), accompanied by one or more minor longer-lived contributions ($\tau_2 \sim$ 2.78-19.2 ns) [52].

Despite the pronounced quenching observed in steady-state PL spectra, CO_2-assisted activation does not lead to systematic prolongation of the photoluminescence lifetimes. Under excitation at 325 nm and emission around 460-480 nm, pristine CN exhibits an intensity-weighted average lifetime ($^{inten}\tau_{aver.}$) of 5.9 ns. Upon moderate CO_2 activation, $^{inten}\tau_{aver.}$ increases slightly to 7.8 ns for CN500 and to 10.7-11.4 ns for CN550-CN600, reflecting an increased contribution from slower decay components associated with activation-induced defect states. This trend does not persist at higher activation temperatures: for CN650, $^{inten}\tau_{aver.}$ decreases again to 7.8 ns, while for CN675 it drops further to 4.1 ns, despite the strongest steady-state PL quenching observed for these samples. A similar behaviour is observed for decay profiles recorded at shorter emission wavelengths, which probe higher-energy emission states of the material.

At λ_{em} = 437-440 nm, CN625 and CN650 exhibit increased average lifetimes of 4.16 and 5.23 ns, respectively, whereas CN675 shows a markedly reduced average lifetime of 1.95 ns. At higher-energy emission (λ_{em} = 409 nm), all samples display very short average lifetimes ($^{inten}\tau_{aver.}$ = 0.9-1.4 ns) with only minor variations across the series. This behaviour is consistent with the deconvoluted steady-state PL spectra, where the highest-energy emission component (peak 1) remains essentially unchanged upon CO_2 activation, while the lower-energy emission components evolve significantly. These observations indicate that CO_2 activation mainly affects defect-related recombination pathways, whereas the fastest band-edge recombination processes remain largely unaffected. Importantly, the absence of lifetime extension at high activation temperatures, combined with strong steady-state PL quenching, demonstrates that CO_2-assisted thermal treatment neither suppresses intrinsic radiative recombination nor generates long-lived emissive trap states. Instead, activation-induced defect and edge states primarily serve as efficient non-radiative relaxation or charge-extraction channels [53]. This interpretation is further supported by the increasing dominance of the fast decay component (A_1>90%) in highly activated samples, particularly CN650 and CN675, as shown by the amplitude-weighted

fitting parameters in Table S4.

Dark solid-state X-band EPR spectra of pristine and CO_2-activated g-C_3N_4 samples recorded at room temperature are shown in Fig. 6a. All materials display a single first-derivative EPR signal centred within a narrow g-value range of approximately 2.002 to 2.006, characteristic of unpaired electrons delocalised within the π-conjugated carbon nitride framework and/or associated with intrinsic nitrogen-related defect and edge sites [54]. The absence of additional resonances across the series indicates that CO_2-assisted thermal activation does not introduce new paramagnetic species but instead modulates the population and electronic environment of native spin-active centres inherent to g-C_3N_4. The EPR signal intensity shows a pronounced, non-monotonic dependence on activation temperature. Pristine CN exhibits the weakest signal, consistent with a low concentration and poor accessibility of paramagnetic centres in the bulk, highly stacked framework. Upon CO_2 activation, the EPR intensity increases markedly, reaching a maximum for CN600, indicating the most effective generation or exposure of intrinsic defect-related spin centres under moderate activation conditions. This behaviour reflects controlled exfoliation and internal etching of the carbon nitride framework, which enhances the accessibility of electronically active edge and defect sites while preserving sufficient π-electronic conjugation to support spin delocalisation [38]. Consistent with XPS results showing preserved nitrogen chemical states up to 650 °C, this behaviour confirms that CO_2 activation primarily increases the density and accessibility of electronically active defect centres without causing large-scale chemical reconstruction of the carbon nitride framework.

At higher activation temperatures, the EPR intensity decreases for CN650 and CN675, indicating progressive disruption of long-range electronic coherence and partial degradation of the conjugated network. This decrease parallels the strong quenching of steady-state photoluminescence, the collapse of individual emission components revealed by Gaussian deconvolution, and the shortening of charge-carrier lifetimes observed by TCSPC for highly activated samples. The combined spectroscopic evidence thus indicates that excessive CO_2 activation does not further increase the density of electronically effective defect centres but instead promotes their electronic decoupling and the dominance of non-radiative relaxation pathways. Importantly, the g-value position and overall spectral shape remain essentially unchanged across the activation series, demonstrating that the chemical nature of the paramagnetic centres is preserved and that CO_2-assisted activation primarily affects their density, accessibility, and electronic coupling,

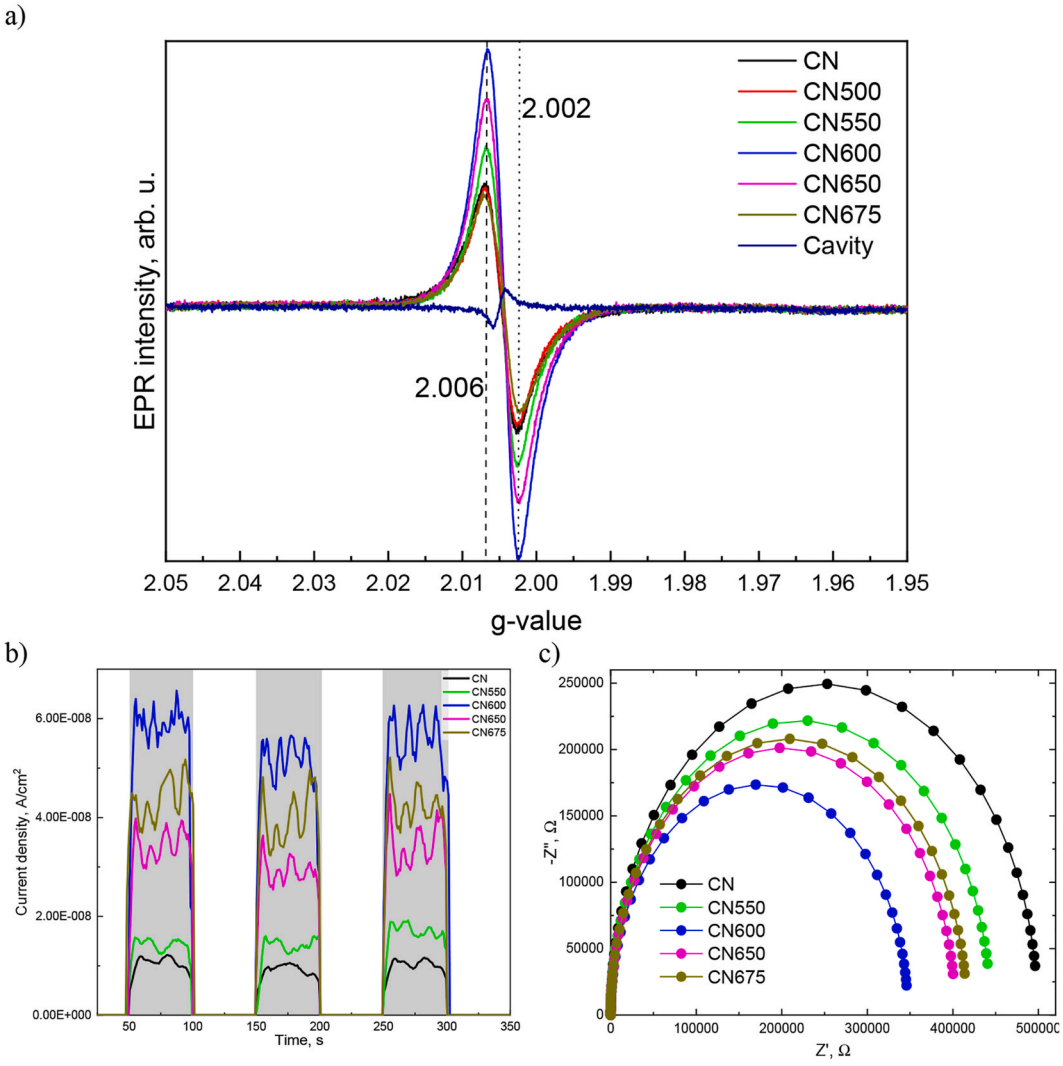

Fig. 6. a) Solid-state EPR spectra of pristine and CO_2-activated g-C_3N_4 samples recorded in the dark at room temperature. All samples display a characteristic single-line signal centred at g = 2.003, attributed to intrinsic carbon- and nitrogen-related paramagnetic defect centres. The dashed lines indicate the g-values used for comparison, and the cavity spectrum is shown as a reference. b) Transient photocurrent responses of pristine and CO_2-activated g-C_3N_4 photoelectrodes recorded under visible-light illumination (grey area). c) Nyquist plots from electrochemical impedance spectroscopy showing the activation-dependent evolution of interfacial charge transfer resistance.

rather than introducing new defect types. In this context, the maximum EPR intensity observed for CN600 identifies an optimal defect density regime, in which intrinsic spin-active centres are sufficiently abundant and electronically connected to facilitate charge separation without inducing excessive structural or electronic disorder.

To further investigate the photoresponse of the intrinsic paramagnetic centres, solid-state EPR spectra were recorded under visible-light illumination and compared with spectra obtained in the dark (Fig. S18). Upon illumination, all samples show a clear change in EPR signal intensity, while the g-value position and overall spectral line shape remain essentially unchanged. This behaviour indicates that light exposure modulates the population of pre-existing spin-active centres rather than generating new paramagnetic species [48]. Notably, the magnitude of the light-induced EPR response depends strongly on the CO_2 activation temperature and is most pronounced for the highly activated samples CN650 and CN675, which show the largest light-dark intensity difference. This observation indicates that illumination leads to a strong modulation of paramagnetic centre populations in these materials, consistent with a high density of electronically accessible states that respond to photoexcitation. CN600 also shows a distinct photoresponse, confirming efficient photoactivity in the optimal activation regime; however, its light-dark intensity difference is smaller than that observed for CN650 and CN675. Importantly, the unchanged g-values under illumination further confirm that CO_2 activation does not alter the chemical identity of the paramagnetic centres. Instead, CO_2-assisted activation predominantly controls their population and photoresponsiveness, which evolve non-monotonically across the activation series. Considered together with excitation-dependent PL and TCSPC results, the light-induced EPR response highlights that strong photoinduced spin modulation can occur even in highly activated samples, while other spectroscopic metrics (PL intensity, decay dynamics, and dark EPR trends) capture the balance between defect generation and preservation of electronic coherence.

Taken together, the spectroscopic analyses demonstrate that CO_2-assisted thermal activation systematically tunes the optical and electronic properties of g-C_3N_4 while preserving the chemical identity of the framework up to CN650. Progressive defect formation enhances visible-light absorption and promotes efficient charge separation; however, excessive activation leads to dominant non-radiative relaxation and progressive loss of long-range electronic coherence. Consequently, the optimum electronic functionality is observed for CN600, where electronically accessible defect states remain effectively coupled within the conjugated carbon nitride framework. These findings demonstrate that the electronic properties of CO_2-activated g-C_3N_4 are governed by the balance between defect generation and preservation of electronic coherence rather than by maximisation of defect density alone.

3.4. Photoelectrochemical properties and interfacial charge transfer

The photoelectrochemical behaviour of pristine and CO_2-activated g-C_3N_4 photoelectrodes was investigated by transient photocurrent measurements and electrochemical impedance spectroscopy (EIS) under visible-light irradiation to elucidate the activation-dependent evolution of charge separation, transport, and interfacial charge-transfer processes. Transient photocurrent responses recorded under chopped visible-light illumination (Fig. 6b) reveal a clear and reproducible photoresponse for all CO_2-activated samples, whereas pristine CN exhibits only a weak current density. The steady-state photocurrent shows a pronounced non-monotonic dependence on the CO_2 activation temperature, following the order CN600 > CN650 ≥ CN675 > CN550 > CN. The highest photocurrent observed for CN600 indicates the most favourable balance between photogenerated charge separation and long-range charge transport through the g-C_3N_4 film. In contrast, although CN650 and CN675 exhibit enhanced visible-light absorption and a higher density of activation-induced defect states, their photocurrent responses are lower than that of CN600, indicating that excessive defect formation may introduce additional charge-trapping sites. The comparatively lower photocurrent of CN550 reflects insufficient electronic tuning at lower activation temperatures, despite largely preserved structural coherence.

Electrochemical impedance spectroscopy provides quantitative support for these trends. Nyquist plots recorded under visible-light irradiation (Fig. 6c) display depressed semicircles characteristic of non-ideal interfacial charge-transfer behaviour [55]. The spectra were fitted using the equivalent electrical circuit shown in Fig. S19, consisting of the solution resistance (R_S) in series with a parallel combination of the charge-transfer resistance (R_{CT}) and a constant phase element (CPE), accounting for surface heterogeneity and distributed capacitive behaviour of the porous g-C_3N_4 films [56]. The extracted R_{CT} values (Table 3) show a clear activation-dependent trend. CN600 exhibits the lowest charge-transfer resistance (0.347 MΩ), confirming the most efficient interfacial electron transfer. This is followed by CN650 (0.403 MΩ) and CN675 (0.416 MΩ), while higher resistances are observed for CN550 (0.443 MΩ) and pristine CN (0.498 MΩ), indicating progressively hindered charge transfer at the electrode-electrolyte interface. The relatively high absolute R_{CT} values are characteristic of polymeric g-C_3N_4 photoelectrodes and reflect their intrinsically low electrical conductivity [26]. Importantly, the EIS-derived charge-transfer resistances mirror the photocurrent response, demonstrating that the steady-state photocurrent is governed primarily by interfacial charge-transfer kinetics rather than by light absorption or defect density alone. The photoelectrochemical results are fully consistent with the spectroscopic analyses presented in Section 3.3, identifying CN600 as the optimum activation regime for charge separation and interfacial charge transport. However, photoelectrochemical measurements probe efficient carrier extraction to an electrode, whereas slurry photocatalysis depends on local charge consumption at the catalyst surface. Consequently, the relationship between the photoelectrochemical response and the photocatalytic performance is discussed in the following sections.

3.5. Photocatalytic degradation of bisphenols and surface-driven reaction mechanism

The photocatalytic activity of pristine and CO_2-activated g-C_3N_4 samples was evaluated using bisphenol A (BPA) as a representative organic pollutant under visible-light irradiation in aqueous suspension. Before illumination, all experiments included a dark equilibration period to establish adsorption-desorption equilibrium and to distinguish purely adsorptive contributions from photoinduced degradation processes. As shown in Fig. 7a, a partial decrease in BPA concentration is already observed during the dark adsorption period, particularly for strongly CO_2-activated samples such as CN650 and CN675 (Table S2). This behaviour reflects enhanced adsorption on defect- and edge-rich surfaces generated by CO_2-assisted thermal activation. Importantly, this dark adsorption is not merely a pre-equilibrium artefact but is a key prerequisite for efficient photocatalysis, as it preconcentrates BPA molecules in the immediate vicinity of photoactive surface sites [57]. The increased adsorption capacity is consistent with the higher accessibility of nitrogen-based surface functionalities identified by ATR-FTIR, pyridine-TPD, and zeta potential analyses. These surface sites may enhance interactions between the catalyst surface and BPA molecules, thereby promoting photocatalytic reactions.

Upon visible-light irradiation, BPA degradation proceeds well beyond the adsorption equilibrium for all activated samples, confirming that BPA removal is dominated by photocatalytic reactions rather than adsorption alone. Pristine CN shows negligible activity under illumination, whereas CO_2-activated samples exhibit substantially enhanced degradation. The activity follows a clear activation-temperature-dependent trend, with CN650 displaying the highest BPA degradation efficiency, followed by CN675, CN625, CN600, CN550, and CN500. This non-monotonic behaviour evidences the existence of an optimal activation window in which surface functionality, electronic structure, and

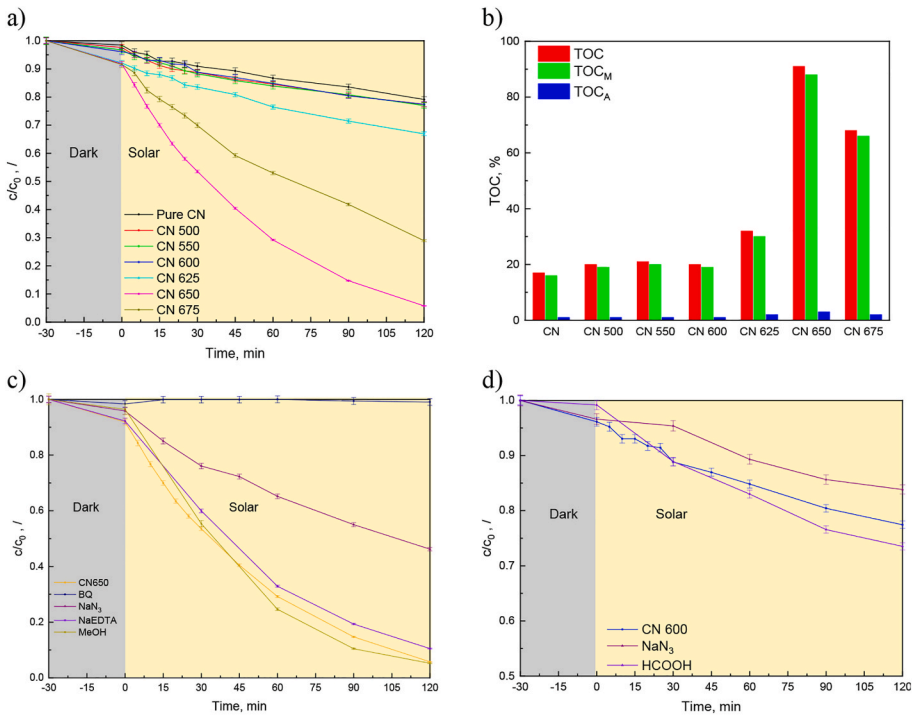

Fig. 7. a) Photocatalytic degradation of bisphenol A (BPA) dissolved in water under simulated solar irradiation using pristine and CO_2-treated CN samples. The suspension was stirred in the dark for 30 min before illumination to establish adsorption-desorption equilibrium. b) Total organic carbon (TOC) removal, mineralised carbon (TOC_M), and organic carbon accumulated on the catalyst surface (TOC_A) after 120 min of irradiation, highlighting mineralisation efficiency. c-d) Scavenger experiments conducted under identical conditions reveal superoxide-radical-driven oxidation pathways, with CN650 showing enhanced reactive oxygen species generation and charge-carrier utilisation compared to CN600. Error bars represent the standard deviation obtained from three independent experiments (n = 3).

charge utilisation are favourably balanced. To quantitatively compare the photocatalytic performance of the samples investigated, the BPA degradation data were further analysed using a pseudo-first-order kinetic model (Fig. S20). The apparent reaction rate constants (k_{app}), obtained from the linear relationship between $\ln(C_0/C)$ and irradiation time, are summarised in Table S6. The kinetic analysis closely follows the degradation trends observed in Fig. 7a, with CN650 exhibiting the highest apparent reaction rate constant (2.23×10^{-2} min^{-1}), followed by CN675 (9.32×10^{-3} min^{-1}), whereas pristine CN and the mildly activated samples displayed substantially lower values (1.67-2.66×10^{-3} min^{-1}). These results further confirm that CN650 provides the optimum balance between activation-induced defect formation and the preservation of long-range electronic coherence, resulting in the most efficient photocatalytic degradation of BPA.

To further clarify the extent of pollutant mineralisation, total organic carbon (TOC) measurements were combined with CHNS elemental analysis of fresh and spent catalysts (Fig. 7b). The reported mineralisation efficiencies are based on TOC analysis of the liquid phase and therefore reflect the removal of dissolved organic carbon under the applied photocatalytic conditions. The total TOC removal can be divided into two contributions: estimated mineralisation (TOC_M), estimated from the combined TOC and CHNS analyses, and carbon accumulation on the catalyst surface (TOC_A), quantified from the difference in carbon content between fresh and used catalysts. For all samples investigated, TOC_A remains very low (1-3%), indicating negligible accumulation of partially oxidised intermediates on the catalyst surface and confirming the absence of significant surface fouling. The dominant fraction of TOC removal is therefore attributed to TOC_M, indicating extensive mineralisation under the applied photocatalytic conditions. The activation-dependent trend in mineralisation closely follows the BPA degradation behaviour. Pristine CN and mildly activated samples (CN500-CN600) exhibit limited TOC removal (17-21%), whereas CN625 shows a moderate increase (32%). CN650 achieved the highest TOC removal (91%), corresponding to the highest mineralisation efficiency among the investigated photocatalysts, with 88% assigned to TOC_M. This result clearly identifies CN650 as the optimal activation regime, where defect-assisted oxygen activation and preserved electronic coherence are most effectively coupled. Although CN675 no longer represents an optimised photocatalyst, its inclusion is essential because it defines the upper limit of beneficial CO_2-assisted activation and provides direct experimental evidence for the transition from beneficial defect formation to excessive framework degradation. Despite maintaining a high mineralisation fraction (68% of the removed TOC, Fig. 7b), its overall mineralisation efficiency remains lower than that of CN650 due to reduced overall BPA degradation. These results suggest that CN650 represents the optimal activation regime, where surface reactivity and electronic coherence are most effectively coupled, enabling near-complete mineralisation rather than partial transformation. Although TOC analysis combined with CHNS measurements provides a quantitative assessment of dissolved organic carbon removal and carbon accumulation on the catalyst surface, detailed identification of soluble degradation intermediates and establishment of a complete carbon mass balance were beyond the scope of the present study. Nevertheless, the very low TOC_A values (1-3%) indicate negligible accumulation of carbonaceous species on the catalyst surface, supporting the conclusion that the observed TOC removal is predominantly associated with mineralisation rather than surface fouling. Further identification of degradation intermediates by LC-MS or GC-MS will be addressed in future studies.

To further benchmark the performance of the CO_2-activated photocatalysts, Table 4 compares the photocatalytic degradation of bisphenol A over recently reported g-C_3N_4-based photocatalysts operating under visible-light irradiation. Most reported strategies enhance photocatalytic activity through heteroatom doping, defect engineering, or thermal exfoliation, which improve visible-light absorption, charge separation, and the availability of catalytically active sites. Although several of these photocatalysts achieve complete BPA degradation, they

Table 4
Comparison of recently reported g-C_3N_4-based photocatalysts for visible-light photocatalytic degradation of bisphenol A with the CO_2-activated g-C_3N_4 photocatalyst developed in the present work.

Photocatalyst	Modification	BPA	Catalyst	Time	k	BPA	TOC	Stability	Ref.
		mg L^{-1}	mg L^{-1}	min	min^{-1}	%	%		
Co-OCNVN	Co/N vacancies	15	400	180	0.0286	100	66	6 cycles	[58]
Oxygen-rich EGCN	Exfoliation	2	500	120	0.0450	100	NR	3 cycles	[59]
Carbon-defect g-C_3N_4	C doping + defects	10	200	90	0.0614	100	60.6	5 cycles	[60]
O-doped porous g-C_3N_4	O doping	30	2500	240	0.0062	82.6	84.3	Stable	[61]
Carbon self-doped g-C_3N_4	C self-doping	10	500	150	0.0180	93.2	27.6	5 cycles	[62]
This work (CN650)	CO_2 activation	10	125	120	0.0223	94.2	91.0	5 cycles	This work

NR - not reported. Apparently first-order rate constants (k) were calculated or reported assuming pseudo-first-order kinetics under the experimental conditions described in the respective references.

generally require substantially higher catalyst loadings (200-2500 mg L^{-1}) than the CO_2-activated photocatalyst developed in the present work. In contrast, CN650 achieves 94.2% BPA degradation together with the highest mineralisation efficiency (91% TOC removal) using a catalyst loading of only 125 mg L^{-1} under visible-light irradiation. Importantly, unlike previous studies that primarily focused on improving photocatalytic performance through structural modification, the present work establishes a comprehensive structure-property-activity relationship by systematically correlating the evolution of the carbon nitride framework with charge-carrier dynamics, reactive oxygen species generation, and photocatalytic activity over a broad CO_2 activation-temperature range. The identification of the defect-coherence crossover demonstrates that optimum photocatalytic performance is governed by the balance between activation-induced defect formation and preservation of the conjugated carbon nitride framework rather than by defect density or reactive oxygen species generation alone. These findings highlight CO_2-assisted thermal activation as a simple, scalable, and sustainable strategy for designing high-performance metal-free photocatalysts for visible-light-driven water purification.

The nature of the reactive species governing BPA degradation was investigated by scavenger experiments (Fig. 7c and d). For CN650, the addition of p-benzoquinone (BQ) almost completely suppresses BPA degradation, confirming superoxide anion radicals ($^{\bullet}O_2^-$) as the primary oxidising species under the applied conditions [63], [64]. Sodium azide (NaN_3) causes substantial but incomplete inhibition, with c/c_0 rising from 0.10 to 0.46 after 120 min, indicating that oxygen-centred reactive pathways contribute to the overall reaction network, potentially involving singlet oxygen species derived from superoxide chemistry. In contrast, MeOH (primarily $^{\bullet}OH$ scavenger) and NaEDTA (hole scavenger) exert only minor influence, demonstrating that hydroxyl radicals and direct hole oxidation play secondary roles. For CN600, the overall degradation extent is considerably lower ($c/c_0 \sim 0.77$ after 120 min), and NaN_3 increases c/c_0 to 0.839. Although the absolute effect is smaller than for CN650, the relative decrease in degradation efficiency is comparable. This indicates that similar reactive oxygen species are involved in both systems. However, their generation and effective utilisation are significantly more efficient in CN650. The difference between CN600 and CN650 therefore does not primarily arise from a change in the identity of the reactive species, but rather from the degree of interfacial coupling between photogenerated charge carriers and oxygen activation sites. Under slurry photocatalytic conditions, efficient BPA degradation is therefore governed mainly by surface-mediated oxygen activation rather than by favourable bulk charge transport characteristics alone.

Direct evidence for reactive oxygen species formation during photocatalysis was obtained from DMPO spin-trapping EPR measurements performed after visible-light irradiation (Fig. S21). All CO_2-activated samples exhibit characteristic multiplet signals corresponding to the DMPO-$^{\bullet}O_2^-$ adduct, whereas pristine CN shows only a weak response [65]. The intensity of the DMPO-derived signal increases with activation temperature, with CN650 and CN675 displaying the strongest generation of superoxide anion radicals. Notably, the photocatalytic activity does not follow the same trend. CN675 produces the highest absolute DMPO-detected superoxide signal; however, its photocatalytic performance remains lower than that of CN650. These results indicate that maximal radical generation does not necessarily translate into optimal photocatalytic performance. Efficient pollutant degradation instead requires balanced coupling between defect-assisted oxygen activation and preserved electronic coherence. This behaviour indicates that excessive activation promotes radical formation but simultaneously introduces structural disorder and recombination pathways, which limit overall catalytic efficiency. The superior performance of CN650 therefore reflects an optimal defect-coherence regime, where substrate adsorption, defect-assisted charge extraction, and superoxide-mediated oxidation are most effectively coupled. The EPR findings corroborate the scavenger-based identification of superoxide radicals as the primary oxidising species governing BPA degradation. The stronger inhibition observed following p-benzoquinone addition for CN600 and CN650 is consistent with the higher DMPO-$^{\bullet}O_2^-$ EPR signal intensity, confirming the dominant role of superoxide anion radicals during BPA degradation. To further evaluate oxygen-centred reactive species, TEMP spin-probe EPR measurements were performed under identical visible-light irradiation conditions (Fig. S22). The characteristic TEMPO triplet confirmed the formation of singlet oxygen ($^1O_2$) for all investigated samples, with the signal intensity increasing in the order CN600 < CN650 < CN675. Similar to the DMPO spin-trapping results, the strongest $^1O_2$ signal was observed for CN675, despite its lower photocatalytic activity compared with CN650. This further demonstrates that enhanced reactive oxygen species generation alone is insufficient to achieve optimal photocatalytic performance and that efficient utilisation of the generated reactive oxygen species is equally important. Although CN675 exhibits the strongest EPR response, its lower photocatalytic activity further demonstrates that reactive oxygen species generation alone is insufficient to achieve optimal photocatalytic performance and must be accompanied by efficient charge utilisation and the preservation of long-range electronic coherence. It should be noted that scavenger experiments are inherently semi-quantitative because the selectivity and reaction kinetics of individual scavengers are not absolute. Therefore, the proposed reaction mechanism is based on the combined evidence obtained from scavenger experiments together with DMPO and TEMP spin-probe EPR, PL, TCSPC, and EIS analyses.

To further connect solid-state spectroscopy with realistic photocatalytic conditions, steady-state PL (Fig. S23) and TCSPC measurements were performed in aqueous suspensions using the same catalyst loading and BPA concentration as in the degradation experiments. PL spectra recorded under excitation at 370 nm and 445 nm show substantially stronger quenching for CN650 compared to CN500, both in pure water and in BPA-containing suspensions, indicating more efficient interfacial charge extraction under reaction-relevant conditions. A direct comparison of the PL response for each catalyst measured in water and in BPA solution further reveals that the presence of BPA induces additional PL quenching relative to water alone, consistent with the opening of substrate-assisted interfacial non-radiative charge-

consumption pathways. Time-resolved PL measurements (Table S4) show that the intensity-weighted average lifetimes remain largely comparable in water and in BPA-containing suspensions, while the relative amplitudes of individual decay components are redistributed. This behaviour indicates a shift from bulk-like radiative recombination pathways towards surface-mediated non-radiative extraction channels, rather than a systematic prolongation of intrinsic radiative lifetimes.

To clarify the role of dissolved oxygen in interfacial charge-consumption processes, additional TCSPC measurements were conducted for CN500 in water after removing dissolved O_2 by purging the suspension with N_2, which reduced the oxygen concentration from 8.14 to 0.26 mg L^{-1} (Table S5). The decay profiles recorded under oxygen-depleted conditions closely resembled those measured in aerated water, with only minor changes in the average lifetime and relative decay amplitudes. This behaviour indicates that dissolved oxygen does not dominate the intrinsic radiative recombination dynamics of g-C_3N_4, but instead acts as a competitive surface electron acceptor, diverting photogenerated electrons into oxygen reduction pathways without significantly altering the bulk lifetime. The combined observation of strong PL quenching in the absence of lifetime extension confirms that photogenerated electrons are rapidly consumed at the catalyst-solution interface and diverted into chemical reaction pathways, enabling efficient formation of reactive oxygen species. These trends are fully consistent with DMPO-EPR spin trapping, scavenger experiments, and photocatalytic activity measurements, and further support the conclusion that BPA degradation is governed by fast surface charge utilisation rather than by bulk recombination kinetics.

Photocatalytic degradation of BPA over CO_2-activated g-C_3N_4 arises from the interplay between structural evolution, electronic structure, and interfacial redox processes. CO_2-assisted thermal activation progressively thins the carbon nitride layers, exposes edge terminations, and increases the density of defect-associated sites while largely preserving the heptazine framework. Moderate activation (CN550-CN600) improves charge separation and transport, whereas stronger activation, particularly for CN650, promotes rapid extraction of photogenerated electrons to surface oxygen activation sites, as evidenced by pronounced PL quenching together with the absence of lifetime prolongation in TCSPC. These electrons are efficiently transferred to dissolved oxygen, generating superoxide anion radicals that drive BPA oxidation, as confirmed by scavenger experiments and DMPO spin-trapping EPR. The weak correlation between TCSPC lifetimes and photocatalytic activity reflects the fundamentally different processes probed by these techniques: TCSPC measures radiative recombination within the semiconductor, whereas photocatalysis depends on rapid interfacial charge consumption. Although CN675 exhibited the highest specific surface area and the strongest superoxide anion radical generation, these features alone were insufficient to achieve the highest photocatalytic activity. The combined XRD, XPS, PL, TCSPC, EIS, and EPR results demonstrate that excessive CO_2 activation progressively disrupts the graphitic carbon nitride framework, compromising the preservation of long-range electronic coherence within the conjugated network. Consequently, although reactive oxygen species are generated efficiently, their utilisation in photocatalytic oxidation becomes less effective because photogenerated charge carriers experience increased localisation and reduced transport efficiency. In contrast, CN650 represents the optimum balance between activation-induced defect formation and the preservation of the carbon nitride framework, enabling efficient charge separation, charge transport, and ROS utilisation, which ultimately results in the highest BPA degradation and mineralisation efficiency.

This interpretation also explains the apparent discrepancy between the photoelectrochemical properties and the photocatalytic performance of CN600 and CN650. Although CN600 exhibited the strongest EPR response, the highest photocurrent density, and the lowest charge-transfer resistance, these parameters alone do not determine the overall photocatalytic performance. Photocatalytic oxidation is governed by the combined influence of charge generation, charge transport, interfacial charge utilisation, reactive oxygen species generation, surface reaction kinetics, and the availability of catalytically active surface sites. Further CO_2 activation from 600 to 650 °C increases the accessibility of defect-associated active sites while largely preserving the conjugated carbon nitride framework and long-range electronic coherence, thereby enabling more efficient utilisation of photogenerated charge carriers for oxygen activation and pollutant oxidation. Consequently, CN650 achieves the highest BPA degradation and mineralisation efficiency despite its slightly lower photocurrent response and EPR intensity compared with CN600. These observations demonstrate that no single photoelectrochemical descriptor can predict photocatalytic performance. Instead, optimum activity arises from the balanced interplay between activation-induced defect formation, preservation of long-range electronic coherence, and efficient interfacial charge utilisation.

Finally, the operational stability of the optimally activated CN650 photocatalyst was evaluated over five consecutive photocatalytic cycles under identical visible-light irradiation conditions (Fig. S24a). After each cycle, the catalyst was recovered by centrifugation, washed with deionised water, dried, and reused without further treatment. The BPA degradation profiles remained nearly unchanged throughout the recycling tests, with no significant decrease in reaction rate or final conversion. Likewise, the TOC removal efficiency remained stable at approximately 88-90% (Fig. S24b), indicating sustained mineralisation performance. The negligible variation in TOC removal and the absence of progressive activity loss confirm that carbon accumulation on the catalyst surface ($TOC_A \leq 3\%$) does not cause catalyst deactivation under the applied reaction conditions. Post-reaction ATR-FTIR and XRD analyses of the recovered CN650 photocatalyst after five consecutive photocatalytic cycles (Fig. S25) revealed no detectable structural changes compared with the fresh material, confirming the excellent structural stability of the graphitic carbon nitride framework. Together with the negligible surface carbon accumulation identified by CHNS analysis, these results demonstrate that the defect-assisted activation regime achieved by CO_2 treatment remains stable during repeated photocatalytic operation. The combined structural, spectroscopic, photoelectrochemical, and photocatalytic results establish a comprehensive structure-property-activity relationship for the CO_2-activated g-C_3N_4 series. Progressive CO_2-assisted activation initially introduces beneficial structural defects that enhance visible-light absorption, facilitate interfacial charge separation, and promote reactive oxygen species generation. At the same time, the conjugated carbon nitride framework remains sufficiently preserved to maintain long-range electronic coherence, enabling efficient charge transport and utilisation. Consequently, CN650 exhibits the optimum balance between activation-induced defect formation and the preservation of the conjugated framework, resulting in the highest BPA degradation and mineralisation efficiency. Further activation to 675 °C continues to increase defect density and superoxide radical generation; however, extensive framework degradation progressively compromises the preservation of long-range electronic coherence, leading to increased carrier localisation, reduced charge transport, and less efficient utilisation of the generated reactive oxygen species. These findings demonstrate that photocatalytic performance is governed not simply by defect density, surface area, or reactive oxygen species generation, but by the balance between beneficial defect formation and preservation of the conjugated carbon nitride framework.

4. Conclusions

Controlled defect engineering represents an effective strategy for improving the performance of metal-free photocatalysts. In this study, CO_2-assisted thermal activation is demonstrated as a controllable and scalable approach for tuning the structural, electronic, and photocatalytic properties of graphitic carbon nitride within a well-defined activation window. Systematic variation of the activation temperature

between 500 and 675 °C revealed three distinct regimes governing the evolution of the material. Moderate activation preserves the conjugated carbon nitride framework while introducing beneficial structural defects, whereas excessive activation at 675 °C leads to progressive framework degradation, increased charge-carrier localisation, and loss of long-range electronic coherence. The optimum photocatalytic performance is achieved for CN650, where activation-induced defect formation and preservation of the conjugated framework are most effectively balanced. Under these conditions, efficient interfacial charge utilisation promotes superoxide-mediated oxidation, resulting in the highest BPA degradation and near-complete mineralisation under visible-light irradiation. Importantly, the results demonstrate that photocatalytic performance is governed not simply by defect density, surface area, or reactive oxygen species generation, but by the balance between beneficial defect formation and preservation of long-range electronic coherence.

The comprehensive combination of structural, spectroscopic, photoelectrochemical, and photocatalytic analyses establishes a clear structure-property-activity relationship for CO_2-activated g-C_3N_4 and introduces the concept of a defect-coherence crossover as a useful framework for understanding and designing defect-engineered metal-free photocatalysts. More broadly, this work highlights CO_2-assisted activation as a scalable and sustainable strategy for tailoring visible-light-responsive photocatalysts for environmental remediation. Although the present study was performed using model bisphenol pollutants under controlled laboratory conditions, the mechanistic insights obtained here provide a rational basis for the future development and evaluation of CO_2-activated graphitic carbon nitride photocatalysts for more complex water-treatment applications.

CRediT authorship contribution statement

Gregor Žerjav: Conceptualization, Investigation, Supervision, Validation, Visualization, Writing – original draft, Writing – review & editing. **Matevž Roškarič:** Conceptualization, Investigation, Visualization, Writing – original draft, Writing – review & editing. **Andraž Mavrič:** Investigation, Visualization. **Miklós Németh:** Investigation, Visualization. **Albin Pintar:** Investigation, Resources, Validation, Writing – original draft, Writing – review & editing.

Declaration of competing interest

The authors declare that they have no known competing financial interests or personal relationships that could have appeared to influence the work reported in this paper.

Acknowledgements

The authors would like to express their gratitude to the Slovenian Research and Innovation Agency for providing financial support through research core funding under grant P2-0150.

Appendix A. Supplementary data

Supplementary data to this article can be found online at https://doi.org/10.1016/j.mtsust.2026.101422.

Data availability

Data will be made available on request.

References

[1] G. Žerjav, J. Teržan, P. Djinović, Z. Barbieriková, T. Hajdu, V. Brezová, J. Zavašnik, J. Kovač, A. Pintar, TiO_2-β-Bi_2O_3 junction as a leverage for the visible-light activity of TiO_2 based catalyst used for environmental applications, Catal. Today 361 (2021) 165–175, https://doi.org/10.1016/j.cattod.2020.03.053.

[2] B. Cojocaru, V. Andrei, M. Tudorache, F. Lin, C. Cadigan, R. Richards, V. I. Parvulescu, Enhanced photo-degradation of bisphenol pollutants onto gold-modified photocatalysts, Catal. Today 284 (2017) 153–159, https://doi.org/10.1016/j.cattod.2016.11.009.

[3] S. Foteinis, E. Chatzisymeon, Heterogeneous photocatalysis for water purification, in: Nanostructured Photocatalysts, Elsevier, 2020, pp. 75–97, https://doi.org/10.1016/B978-0-12-817836-2.00004-1.

[4] V. Loddo, M. Bellardita, G. Camera-Roda, F. Parrino, L. Palmisano, Heterogeneous photocatalysis, in: Current Trends and Future Developments on (Bio-) Membranes, Elsevier, 2018, pp. 1–43, https://doi.org/10.1016/B978-0-12-813549-5.00001-3.

[5] M. Chu, J. Zhao, M. Zou, W. Xing, Y. Liu, Advances on biochar applications for organic wastewater treatment: material design, removal mechanisms, innovative machine learning and challenges, Environ. Res. 286 (2025) 122967, https://doi.org/10.1016/j.envres.2025.122967.

[6] A.S. Ansari, G. Azzahra, F.G. Nugroho, M.M. Mujtaba, A.T.A. Ahmed, Oxides and metal oxide/carbon hybrid materials for efficient photocatalytic organic pollutant removal, Catalysts 152 (2025) 134, https://doi.org/10.3390/catal15020134.

[7] Y. Jari, N. Najid, M.C. Necibi, B. Gourich, C. Vial, A. Elhalil, P. Kaur, I. Mohdeb, Y. Park, Y. Hwang, A. Ruiz Garcia, N. Roche, A. El Midaoui, A comprehensive review on TiO_2-based heterogeneous photocatalytic technologies for emerging pollutants removal from water and wastewater: from engineering aspects to modeling approaches, J. Environ. Manag. 373 (2025) 123703, https://doi.org/10.1016/j.jenvman.2024.123703.

[8] M. Roškarič, G. Žerjav, J. Zavašnik, A. Pintar, The influence of synthesis conditions on the visible-light triggered photocatalytic activity of g-C_3N_4/TiO_2 composites used in AOPs, J. Environ. Chem. Eng. 10 (2022) 107656, https://doi.org/10.1016/j.jece.2022.107656.

[9] M. Roškarič, J. Zavašnik, D. Zámbó, T. Kotnik, S. Kovačič, G. Žerjav, A. Pintar, Optimization method based on simplex for surface area improved photocatalytic performance of g-C_3N_4, ACS Catal. 13 (2023) 13282–13300, https://doi.org/10.1021/acscatal.3c03394.

[10] W. Sun, J. Zhu, Y. Zheng, Graphitic carbon nitride heterojunction photocatalysts for solar hydrogen production, Int. J. Hydrogen Energy 46 (75) (2021) 37242–37267, https://doi.org/10.1016/j.ijhydene.2021.09.019.

[11] M. Roškarič, G. Žerjav, M. Finšgar, J. Zavašnik, A. Pintar, Influence of the calcination duration of g-C_3N_4/TiO_2 "veggie-toast-like" photocatalyst on the visible-light triggered photocatalytic oxidation of bisphenol A, J. Alloys Compd. 947 (2023) 169585, https://doi.org/10.1016/j.jallcom.2023.169585.

[12] I. Benisti, F. Shaik, Z. Xing, A. Ben-refael, L. Amirav, Y. Paz, The effect of Pt cocatalyst on the performance and transient IR spectrum of photocatalytic g-C_3N_4 nanospheres, Appl. Surf. Sci. 542 (2021) 148432, https://doi.org/10.1016/j.apsusc.2020.148432.

[13] M. Ismael, A review on graphitic carbon nitride (g-C_3N_4) based nanocomposites: synthesis, categories, and their application in photocatalysis, J. Alloys Compd. 846 (2020) 156446, https://doi.org/10.1016/j.jallcom.2020.156446.

[14] Z. Chen, S. Zhang, Y. Liu, N. Saleh Alharbi, S. Omar Rabah, S. Wang, X. Wang, Synthesis and fabrication of g-C_3N_4-based materials and their application in elimination of pollutants, Sci. Total Environ. 731 (2020) 139054, https://doi.org/10.1016/j.scitotenv.2020.139054.

[15] T. Bao, X. Li, S. Li, H. Rao, X. Men, P. She, J. Qin, Recent advances of graphitic carbon nitride (g-C_3N_4) based materials for photocatalytic applications: a review, Nano Mater. Sci. 7 (2025) 145–168, https://doi.org/10.1016/j.nanoms.2024.04.002.

[16] T. Zhong, W. Huang, Z. Yao, X. Long, W. Qu, H. Zhao, S. Tian, D. Shu, C. He, Engineering of graphitic carbon nitride (g-C_3N_4) based photocatalysts for atmospheric protection: modification strategies, recent progress, and application challenges, Small 20 (2024) 2404696, https://doi.org/10.1002/smll.202404696.

[17] S. Hou, X. Gao, X. Lv, Y. Zhao, X. Yin, Y. Liu, J. Fang, X. Yu, X. Ma, T. Ma, D. Su, Decade milestone advancement of defect-engineered g-C_3N_4 for solar catalytic applications, Nano-Micro Lett. 16 (2024) 70, https://doi.org/10.1007/s40820-023-01297-x.

[18] Y. Ruan, Y. Hu, H. Cheng, H. Recent, Progress in g-C_3N_4-Based photocatalysts for organic pollutant degradation: strategies to improve photocatalytic activity, Catalysts 15 (2025) 148, https://doi.org/10.3390/catal15020148.

[19] A. Ali, W.C. Oh, Preparation of nanowire like WSe_2-Graphene nanocomposite for photocatalytic reduction of CO_2 into CH_3OH with the presence of sacrificial agents, Sci. Rep. 7 (2017) 1867, https://doi.org/10.1038/s41598-017-02075-7.

[20] H. Akbar, M.S. Javed, S.T. Iqbal, M.I. Khan, T. Anwar, F. Anjum, A. Ahmad, M. Muneeb, A. Ali, W.-C. Oh, A review of photocatalytic CO_2 reduction: exploring sustainable carbon emission mitigation from thermodynamics to kinetics and strategies for enhanced efficiency, J. Korean Ceram. Soc. 61 (2024) 367–390, https://doi.org/10.1007/s43207-024-00365-1.

[21] M.R.U.D. Biswas, A. Ali, K.Y. Cho, W.-C. Oh, Novel synthesis of WSe_2-Graphene-TiO_2 ternary nanocomposite via ultrasonic technics for high photocatalytic reduction of CO_2 into CH_3OH, Ultrason. Sonochem. 42 (2018) 738–746, https://doi.org/10.1016/j.ultsonch.2017.12.030.

[22] M.F. Vega, C. Olivas, E. Díaz-Faes, C. Barriocanal, Evaluation of water splitting efficiency of g-C_3N_4 thermally etched/exfoliated under air and CO_2 atmospheres, Catal. Today 427 (2024) 114412, https://doi.org/10.1016/j.cattod.2023.114412.

[23] M. Gaidi, M. Al Ali, K. Ramachandran, V.i Vel Rajankumar, S. Columbus, S. Chidambaramc, K. Daoudi, Engineering 2D g-C_3N_4 for enhanced photocatalytic water purification: the impact of post-processing on activity enhancement, Nanoscale 17 (2025) 24017, https://doi.org/10.1039/D5NR02038G.

[24] L. Ni, Y. Xiao, X. Zhou, Y. Jiang, Y. Liu, W. Zhang, J. Zhang, Z. Liu, Significantly enhanced photocatalytic performance of the g-C_3N_4/Sulfur-Vacancy-Containing $Zn_3In_2S_6$ heterostructure for photocatalytic H_2 and H_2O_2 generation by coupling

defects with heterojunction engineering, Inorg. Chem. 61 (2022) 19552–19566, https://doi.org/10.1021/acs.inorgchem.2c03491.
[25] J.M. Zhao, R. Wang, L.L. Wang, T. Wang, Y.P. Pan, X.H. Shui, Y. Sun, The effect of calcination temperature and atmosphere on the photocatalytic properties of g-C_3N_4, Dig. J. Nanomater. Biostruct. 20 (4) (2025) 1275–1283, https://doi.org/10.15251/DJNB.2025.204.1275.
[26] J. Xu, M. Fujitsuka, S. Kim, Z. Wang, T. Majima, Unprecedented effect of CO_2 calcination atmosphere on photocatalytic H_2 production activity from water using g-C_3N_4 synthesized from triazole polymerization, Appl. Catal. B Environ. 241 (2019) 141–148, https://doi.org/10.1016/j.apcatb.2018.09.023.
[27] Y. Lu, C. Liu, L. Zheng, F. Chen, J. Qian, X. Meng, Z. Chen, S. Zhong, B. He, N_3C-Defect-Tuned g-C_3N_4 photocatalysts: structural optimization and enhanced tetracycline degradation performance, Nanomaterials 15 (2025) 466, https://doi.org/10.3390/nano15060466.
[28] A. Alaghmandfard, K. Ghandi, Comprehensive review of graphitic carbon nitride (g-C_3N_4)–Metal oxide-based nanocomposites: potential for photocatalysis and sensing, Nanomaterials 12 (2022) 294, https://doi.org/10.3390/nano12020294.
[29] X. Wang, K. Maeda, A. Thomas, K. Takanabe, G. Xin, J.M. Carlsson, K. Domen, M. Antonietti, A metal-free polymeric photocatalyst for hydrogen production from water under visible light, Nat. Mater. 8 (2009) 76–80, https://doi.org/10.1038/nmat2317.
[30] J. Liu, H. Wang, M. Antonietti, Graphitic carbon nitride “reloaded”: emerging applications beyond (photo)catalysis, Chem. Soc. Rev. 45 (2016) 2308–2326, https://doi.org/10.1039/C5CS00767D.
[31] A. Thomas, A. Fischer, F. Goettmann, M. Antonietti, J.-O.l Müller, R. Schlöglb, J. M. Carlsson, Graphitic carbon nitride materials: variation of structure and morphology and their use as metal-free catalysts, J. Mater. Chem. 18 (2008) 4893–4908, https://doi.org/10.1039/B800274F.
[32] M. Thommes, K. Kaneko, A.V. Neimark, J.P. Olivier, F. Rodriguez-Reinoso, J. Rouquerol, K.W. Sing, Physisorption of gases, with special reference to the evaluation of surface area and pore size distribution (IUPAC technical report), Pure Appl. Chem. 87 (2015) 1051–1069, https://doi.org/10.1515/pac-2014-1117.
[33] W.-J. Ong, L.-L. Tan, Y.H. Ng, S.-T. Yong, S.-P. Chai, Graphitic carbon nitride (g-C_3N_4)-Based photocatalysts for artificial photosynthesis and environmental remediation: are we a step closer to achieving sustainability? Chem. Rev. 116 (2016) 7159–7329, https://doi.org/10.1021/acs.chemrev.6b00075.
[34] Edwin Kroke, Marcus Schwarz, Novel group 14 nitrides, Coord. Chem. Rev. 248 (5–6) (2004) 493–532, https://doi.org/10.1016/j.ccr.2004.02.001.
[35] Y. Zhang, T. Mori, L. Niu, J. Ye, Non-covalent doping of graphitic carbon nitride polymer with graphene: controlled electronic structure and enhanced optoelectronic conversion, Energy Environ. Sci. 4 (2011) 4517–4521, https://doi.org/10.1039/C1EE01400E.
[36] X. Li, J. Zhang, L. Shen, Y. Ma, W. Lei, Q. Cui, G. Zou, Preparation and characterization of graphitic carbon nitride through pyrolysis of melamine, Appl. Phys. A 94 (2009) 387–392, https://doi.org/10.1007/s00339-008-4816-4.
[37] J. Zhang, Y. Chen, X. Wang, Two-dimensional covalent carbon nitride nanosheets: synthesis, functionalization, and application, Energy Environ. Sci. 8 (2015) 3092–3108, https://doi.org/10.1039/C5EE01895A.
[38] Y. Wang, X. Wang, M. Antonietti, Polymeric graphitic carbon nitride as a heterogeneous organocatalyst: from photochemistry to multipurpose catalysis to sustainable chemistry, Angew. Chem. Int. Ed. 51 (2012) 68–89, https://doi.org/10.1002/anie.201101182.
[39] E.A. Kraut, R.W. Grant, J.R. Waldrop, S.P. Kowalczyk, Precise determination of the valence-band edge in X-Ray photoemission spectra: application to measurement of semiconductor interface potentials, Phys. Rev. Lett. 44 (1980) 1620, https://doi.org/10.1103/PhysRevLett.44.1620.
[40] Y. Xu, M.A.A. Schoonen, The absolute energy positions of conduction and valence bands of selected semiconducting minerals, Am. Mineral. 85 (2000) 543–556, https://doi.org/10.2138/am-2000-0416.
[41] P. Niu, L. Zhang, G. Liu, H.-M.i Cheng, Graphene-like carbon nitride nanosheets for improved photocatalytic activities, Adv. Funct. Mater. 22 (2012) 4763–4770, https://doi.org/10.1002/adfm.201200922.
[42] M. Kosmulski, Surface Charging and Points of Zero Charge, CRC Press, 2009, https://doi.org/10.1201/9781420051896.
[43] G.A. Parks, The isoelectric points of solid oxides, solid hydroxides, and aqueous hydroxo complex systems, Chem. Rev. 62 (1965) 177–198, https://doi.org/10.1021/cr60234a002.
[44] X. Wang, X. Chen, A. Thomas, X. Fu, M. Antonietti, Metal-containing carbon nitride compounds: a new functional organic–metal hybrid material, Adv. Mater. 21 (2009) 1609–1612, https://doi.org/10.1002/adma.200802627.
[45] J. Tauc, R. Grigorovici, A. Vancu, Optical properties and electronic structure of amorphous germanium, Phys. Status Solidi 15 (1966) 627–637, https://doi.org/10.1002/pssb.19660150224.
[46] G. Zhang, J. Zhang, M. Zhang, X. Wang, Polycondensation of thiourea into carbon nitride semiconductors as visible light photocatalysts, J. Mater. Chem. 22 (2012) 8083–8091, https://doi.org/10.1039/C2JM00097K.
[47] Y.-Z. Huang, Y.-S. Lin, Y.-S. Lin, T.-C. Chiu, C.-C. Hu, Phosphorus-doped carbon nitride materials for enhanced photocatalytic degradation of organic pollutants under visible-light, ACS Omega 36 (2025) 41457–41466, https://doi.org/10.1021/acsomega.5c04783.
[48] B. Zhu, P. Xia, W. Ho, J. Yu, Isoelectric point and adsorption activity of porous g-C_3N_4, Appl. Surf. Sci. 340 (2015) 188–195, https://doi.org/10.1016/j.apsusc.2015.03.086.
[49] Z. Zhao, Y. Sun, F. Dong, Graphitic carbon nitride based nanocomposites: a review, Nanoscale 7 (2015) 15–37, https://doi.org/10.1039/C4NR03008G.
[50] F. Dong, Y. Li, Z. Wang, W.-K. Ho, Enhanced visible light photocatalytic activity and oxidation ability of porous graphene-like g-C_3N_4 nanosheets via thermal exfoliation, Appl. Surf. Sci. 358 (2015) 393–403, https://doi.org/10.1016/j.apsusc.2015.04.034.
[51] S.C. Yan, Z.S. Li, Z.G. Zou, Photodegradation performance of g-C_3N_4 fabricated by directly heating melamine, Langmuir 25 (2009) 10397–10401, https://doi.org/10.1021/la900923z.
[52] G. Zhang, Z.-A. Lan, X. Wang, Conjugated polymers: catalysts for photocatalytic, hydrogen evolution, Angew. Chem. Int. Ed. 55 (2016) 15712–15727, https://doi.org/10.1002/anie.201607375.
[53] J. Zhang, M. Zhang, R.-Q. Sun, X. Wang, A facile band alignment of polymeric carbon nitride semiconductors to construct isotype heterojunctions, Angew. Chem. Int. Ed. 124 (2012) 10292–10296, https://doi.org/10.1002/ange.201205333.
[54] Y. Zhang, T. Mori, J. Ye, M. Antonietti, Phosphorus-doped carbon nitride solid: enhanced electrical conductivity and photocurrent generation, J. Am. Chem. Soc. 132 (2010) 6294–6295, https://doi.org/10.1021/ja101749y.
[55] A.J. Bard, L.R. Faulkner, H.S. White, Electrochemical Methods: Fundamentals and Applications, third ed., John Wiley & Sons, 2022.
[56] A. Lasia, Electrochemical Impedance Spectroscopy and its Applications, Springer, New York, NY, 2014, https://doi.org/10.1007/978-1-4614-8933-7.
[57] J.-M. Herrmann, Heterogeneous photocatalysis: fundamentals and applications to the removal of various types of aqueous pollutants, Catal. Today 53 (1999) 115–129, https://doi.org/10.1016/S0920-5861(99)00107-8.
[58] Y. Yu, S. Wu, J. Gu, R. Liu, Z. Wang, H. Chen, F. Jiang, Visible-light photocatalytic degradation of bisphenol A using cobalt-tooxygen doped graphitic carbon nitride with nitrogen vacancies via metal-toligand charge transfer, J. Hazard Mater. 384 (2020) 121247, https://doi.org/10.1016/j.jhazmat.2019.121247.
[59] R.S. Sahu, Y. Shih, W.-L. Chen, New insights of metal free 2D graphitic carbon nitride for photocatalytic degradation of bisphenol A, J. Hazard Mater. 402 (2021) 123509, https://doi.org/10.1016/j.jhazmat.2020.123509.
[60] M. Wu, X. He, B. Jing, T. Wang, C. Wang, Y. Qin, Z. Ao, S. Wang, T. An, Novel carbon and defects co-modified g-C_3N_4 for highly efficient photocatalytic degradation of bisphenol A under visible light, J. Hazard. Mater. 384 (2020) 121323, https://doi.org/10.1016/j.jhazmat.2019.121323.
[61] Y. Wei, Y. Liu, C. Liu, X. Li, K. Song, R. Wang, W. Chen, G. Zhao, R. Liu, H. Wang, G. Shi, G. Wang, Oxygen-doped porous g-C_3N_4 via oxalic acid-assisted thermal polycondensation as a visible light-driven photocatalyst for nBisphenol A degradation, ACS Appl. Nano Mater. 6 (2023) 16567–16579, https://doi.org/10.1021/acsanm.3c02762.
[62] L. Lei, X. He, X. Lin, Y. Zhao, C. Yang, L. Cui, G. Wu, Preparation of carbon self-doped g-C_3N_4 for efficient degradation of bisphenol A under visible light irradiation, Environ. Sci. Pollut. Res. 30 (2023) 65328–65337, https://doi.org/10.1007/s11356-023-26928-z.
[63] X. Chen, L. Liu, P.Y. Yu, S.S. Mao, Increasing solar absorption for photocatalysis with black hydrogenated titanium dioxide nanocrystals, Science 331 (2011) 746–750, https://doi.org/10.1126/science.1200448.
[64] F. Dong, L. Wu, Y. Sun, M. Fu, Z. Wu, S.C. Lee, Efficient synthesis of polymeric g-C_3N_4 layered materials as novel efficient visible light driven photocatalysts, J. Mater. Chem. 21 (2011) 15171–15174, https://doi.org/10.1039/C1JM12844B.
[65] E. Finkelstein, G.M. Rosen, E.J. Rauckman, J. Paxton, Spin trapping of superoxide, Mol. Pharmacol. 16 (1979) 676–685, https://doi.org/10.1016/S0026-895X(25)13797-8.